



# Three-dimensional numerical simulation of two-degree-of-freedom VIV of a circular cylinder with varying natural frequency ratios at $Re = 500$

Enhao Wang, Qing Xiao<sup>\*</sup>, Atilla Incecik

Department of Naval Architecture, Ocean and Marine Engineering, University of Strathclyde, Henry Dyer Building, Glasgow G4 0LZ, Scotland, UK



## ARTICLE INFO

### Article history:

Received 24 August 2016  
Received in revised form 1 April 2017  
Accepted 7 June 2017  
Available online 29 June 2017

### Keywords:

Three-dimensional (3D)  
Computational fluid dynamics (CFD)  
Vortex-induced vibration (VIV)  
Two-degree-of-freedom (2DOF)  
Natural frequency ratio

## ABSTRACT

The two-degree-of-freedom (2DOF) vortex-induced vibration (VIV) of a circular cylinder with varying in-line to cross-flow natural frequency ratios ( $f^* = f_{nx}/f_{ny}$ ) is studied using a three-dimensional (3D) computational fluid dynamics (CFD) approach. Numerical simulation is carried out for a constant mass ratio of 2 at a fixed Reynolds number  $Re = 500$ . The reduced velocity ranges from 2 to 12. Three natural frequency ratios are considered, i.e.,  $f^* = 1, 1.5$  and 2. The structural damping is set to zero to maximise the response of the cylinder. The main objective of this study is to investigate the effect of  $f^*$  on the 2DOF VIV responses and the 3D characteristics of the flow. It is discovered that there is a significant increase in the vibration amplitude, and the peak amplitude shifts to a higher reduced velocity when  $f^*$  increases from 1 to 2. A single-peak cross-flow response is observed for the identical in-line and cross-flow mass ratios when  $f^* = 2$ . Dual resonance is found to exist over the range of  $f^*$  studied. The preferable trajectories of the cylinder in the lock-in range are counterclockwise figure-eight orbits. Oblique figure-eight trajectories appear at  $V_r = 6, 7$  and 8 when  $f^* = 1$ . The third harmonic component which is observed in the lift fluctuation increases with  $f^*$ . The correlation decreases in the lock-in range and reaches its minimum value around the transition region between the lock-in and post-lock-in ranges. Three vortex shedding modes (2S, P + S and 2P) appear in the present simulation. A dominant P + S mode is associated with the oblique figure-eight trajectories. Variation of vortex shedding flows along the cylinder is observed leading to the poor correlation of the sectional lift forces.

© 2017 The Authors. Published by Elsevier Ltd. This is an open access article under the CC BY license (<http://creativecommons.org/licenses/by/4.0/>).

## 1. Introduction

Vortex-induced vibration (VIV) of cylindrical structures is a common phenomenon in many engineering applications. Due to its significance, VIV has been extensively studied in recent years. Comprehensive reviews of various aspects of VIV can be found in the publications of Blevins (1977), Williamson and Govardhan (2004), Gabbai and Benaroya (2005), Sumer and Fredsøe (2006), Bearman (2011) and Paidoussis et al. (2014). The preponderance of existing publications have focused on one-degree-of-freedom (1DOF) cross-flow VIV of a circular cylinder (Facchinetti et al., 2004; Farshidianfar and Zanganeh, 2010; Govardhan and Williamson, 2000; Khalak and Williamson, 1999; Sarpkaya, 1995). Nevertheless, several recent experimental studies have revealed the significant effect of the in-line degree of freedom on the VIV response

<sup>\*</sup> Corresponding author.

E-mail address: [qing.xiao@strath.ac.uk](mailto:qing.xiao@strath.ac.uk) (Q. Xiao).

especially when the mass ratio  $m^* = m/(\rho\pi D^2L/4)$  is less than 6 (Blevins and Coughran, 2009; Dahl et al., 2006, 2007, 2010; Jauvtis and Williamson, 2004). Furthermore, studies by Vandiver and Jong (1987), Tognarelli et al. (2004) and Wang and Xiao (2016) have proven that the in-line VIV can contribute as much, or even higher, fatigue damage than the cross-flow VIV to the structures because of the doubled oscillation frequency. Therefore, the number of studies being conducted on two-degree-of-freedom (2DOF) VIV continues to grow (Bai and Qin, 2014; Kang and Jia, 2013; Srinil and Zanganeh, 2012; Srinil et al., 2013; Wu et al., 2016; Zanganeh and Srinil, 2014).

Apart from experiments and semi-empirical modelling, there have been an increasing number of studies on VIV based on the computational fluid dynamics (CFD) tools. The greater part of previous CFD studies on the VIV of a circular cylinder were conducted using two-dimensional (2D) models. Guilmineau and Queutey (2004) presented their simulation results of 1DOF VIV of a circular cylinder, the response of which was well captured in the initial and lower branches. However, the response in the upper branch did not correspond with the experimental results. Singh and Mittal (2005) studied the hysteresis behaviour of 2DOF VIV response of a circular cylinder at low Reynolds numbers (Re). In their study, hysteresis was observed at both the low- and high-ends of the lock-in range and they also observed the P + S vortex shedding mode in free vibration for the first time. Leontini et al. (2006) investigated the branching behaviour of 1DOF VIV at Re = 200. Two response branches similar to the upper and lower branches at higher Re were discovered in their numerical study. The 2D and 3D flow behaviours were also ascertained to have similarities which suggested that the 3D flow branching behaviour has its genesis in the 2D flow. Lucor and Triantafyllou (2008) performed 2D simulation of 2DOF VIV of a circular cylinder in a wide range of in-line to cross-flow natural frequency ratios ( $f^* = f_{nx}/f_{ny}$ ). They observed that the vibration amplitude increases and the peak amplitude shifts to a higher reduced velocity ( $V_r = V/f_{ny}D$ ) as  $f^*$  increases. Zhao and Cheng (2011) simulated 2DOF VIV of a circular cylinder by solving the 2D Reynolds-averaged Navier–Stokes (RANS) equations and reproduced the 2T vortex shedding mode (two triplets of vortices are formed per cycle) and the response in the super-upper branch.

It was found that the flow in the wake of a circular cylinder is three-dimensional (3D) when the Reynolds number exceeds 200 (Williamson, 1988, 1989). Therefore, a series of 3D CFD studies on VIV of a circular cylinder have been conducted. Lucor et al. (2005) presented results of a direct numerical simulation (DNS) of 1DOF VIV and found that there existed a sharp drop in the spanwise correlation of the wake and forces in the region of  $V_r$  around the mode transition between the upper and lower branches. Pontaza and Chen (2006) employed large eddy simulation (LES) and overset (Chimera) grids to study 2DOF VIV of a circular cylinder with low structural mass and damping at  $V_r = 6$  and Re =  $10^5$ . A response characterised by a figure-eight pattern was observed and the vortex shedding exhibited a 2S mode. Saltara et al. (2011) used detached eddy simulation (DES) to simulate 1DOF VIV of a circular cylinder with a low mass-damping parameter at Re =  $10^4$ . In general, their simulation results agreed with the experimental results of Khalak and Williamson (1997), however the vibration amplitudes and force coefficients were overpredicted for  $V_r > 6$ . Kondo (2012), who examined the different excitation mechanisms in the in-line and cross-flow directions based on the numerical results from a 3D computation, captured the first and second excited vibrations of the in-line direction in the  $V_r$  range of  $V_r = 1.7$ – $3.5$  with a low Scruton number ( $Sc = 4\pi m\zeta/(\rho D^2L)$ , where  $\zeta$  is the structural damping ratio). Navrose and Mittal (2013) investigated the transition of responses of 2DOF VIV in the three branches and noted that the cylinder responses and force coefficients exhibited beats in the initial branch. The initial-upper branch transition was found to be hysteretic and intermittency was observed in the transition between the upper and lower branches. Zhao et al. (2014) studied the transition from 2D to 3D for 1DOF VIV of a circular cylinder. In their study, the three-dimensionality of the flow appeared to be strongest in the upper branch and weakest in the initial branch. Additionally, the 2S and 2P vortex shedding modes were acknowledged as coexisting in the upper branch which led to the strong variation of the lift coefficient along the span. Gsell et al. (2016) simulated 2DOF VIV of a circular cylinder at Re = 3900 with direct numerical simulation of the 3D Navier–Stokes equations. The predicted structural responses and forces were consistent with the experimental results reported by Jauvtis and Williamson (2004). The numerical results of this study confirmed the large-amplitude VIV and the shape of the responses. The in-line to cross-flow oscillation frequency ratio was equal to 2 and it was also found that the phase difference between the in-line and cross-flow motions varied across the lock-in range.

The most common scenario for 2DOF VIV is that the in-line and cross-flow natural frequencies are identical (i.e.,  $f_{nx} = f_{ny}$ ). However, it has been previously stressed that cylindrical offshore structures, such as risers, mooring lines and pipelines usually possess an infinite number of natural frequencies in different directions (Srinil et al., 2007; Srinil and Rega, 2007). Therefore, it is of practical interest to study 2DOF VIV with varying  $f^*$ ; particularly, when  $f^* = 2$ , where perfect 2DOF resonance may occur due to the fact that the fluctuating drag oscillates at a frequency twice that of the fluctuating lift. Sarpkaya (1995) and Dahl et al. (2006) observed two-peak cross-flow responses with unequal mass ratios in the in-line and cross-flow directions ( $m_x^* \neq m_y^*$ ) and  $f^*$  around 2. The orbital trajectories and dual resonance of 2DOF VIV of a circular cylinder with varying  $f^*$  were further investigated by Dahl et al. (2010) in subcritical and supercritical Reynolds number ranges. Under dual resonance, the in-line to cross-flow oscillation frequency ratio was found to be  $f_{ox}/f_{oy} \approx 2$  and a third harmonic component was observed in the lift force. A more practical case with  $m_x^* = m_y^*$  and varying  $f^*$  has also been investigated. Srinil et al. (2013) experimentally and numerically studied the 2DOF VIV of a circular cylinder with low mass-damping and varying  $f^*$ . In their study, figure-eight orbital motions were observed for a wide range of  $V_r$  values indicating the occurrence of dual resonance. A flattened single-peak upper branch similar to the experimental results of Assi et al. (2009) was observed when  $f^*$  approaches 2 in their study. Bao et al. (2012) performed a 2D CFD simulation of the 2DOF VIV of a circular cylinder with  $m_x^* = m_y^*$  and varying  $f^*$  at Re = 150. They indicated that dual resonance existed over a wide range of  $f^*$ . A third harmonic frequency component was also observed in the lift fluctuation. Multiple small peaks occurred in the cross-flow response amplitudes of the cylinder when  $f^* = 2$ .

Overall, 1DOF VIV of a circular cylinder has been widely studied during the past few decades. There have also been a number of studies on 2DOF VIV of a circular cylinder; however, most of these focused predominantly on the case of  $f_{ix} = f_{iy}$  with less attention paid to the more practical case with varying  $f^*$ . Existing experimental and numerical investigations on the 2DOF VIV of a circular cylinder with varying  $f^*$  were devoted to the response of the cylinder and 2D flow behaviour. Fully 3D CFD simulations of the 2DOF VIV of a circular cylinder with varying  $f^*$ , which provide detailed information about the transient 3D wake structures, are still quite limited.

In this study, a 3D numerical simulation of the 2DOF VIV of an elastically mounted circular cylinder with mass ratio  $m^* = 2$ , length-to-diameter ratio  $L/D = 12$  and varying  $f^*$  at  $Re = 500$  is conducted. The cylinder is free to vibrate in both the in-line and cross-flow directions. The main objective of the present work is to numerically study a 3D circular cylinder with varying  $f^*$  undergoing 2DOF VIV within an early subcritical  $Re$  regime. Besides the 2DOF VIV responses, there is also a particular focus on aspects such as the correlation lengths and the 3D wake structures which have not been fully addressed by previous studies. It is expected that the 3D CFD modelling could provide more detailed insights into the mechanism of 2DOF VIV.

The arrangement of the paper is as follows. The numerical methods are given in Section 2 and a detailed description of the problem is provided in Section 3. The results and discussions are presented in Section 4 and the conclusions are outlined under Section 5.

## 2. Numerical methods

### 2.1. Flow model

The governing equations for the flow are the 3D unsteady incompressible Navier–Stokes equations. The Arbitrary Lagrangian–Eulerian (ALE) scheme is adopted to solve the governing equations in a moving mesh system. The Navier–Stokes equations in the ALE scheme are expressed as

$$\frac{\partial u_i}{\partial x_i} = 0 \quad (1)$$

$$\frac{\partial u_i}{\partial t} + (u_j - \hat{u}_j) \frac{\partial u_i}{\partial x_j} = -\frac{1}{\rho} \frac{\partial p}{\partial x_i} + \nu \frac{\partial^2 u_i}{\partial x_j^2} \quad (2)$$

where  $x_i$  ( $x_1 = x$ ,  $x_2 = y$ ,  $x_3 = z$ ) represents the Cartesian coordinate,  $u_i$  is the fluid velocity component in the  $x_i$ -direction,  $t$  is the time,  $\hat{u}_i$  is the grid velocity component in the  $x_i$ -direction,  $\rho$  is the fluid density,  $p$  is the pressure and  $\nu$  is the kinematic viscosity of the fluid.

The flow field is simulated using the commercial software package ANSYS CFX (version 15.0) (ANSYS Inc., 2013). The governing equations are discretised using an element-based finite volume method (FVM). Rhie–Chow interpolation is used to obtain the pressure–velocity coupling on collocated grids. A second-order backward Euler scheme is adopted for the temporal discretisation and a high resolution scheme is used as the convective scheme.

### 2.2. Structural model

According to Zhao and Cheng (2011), the 2DOF motion of an elastically mounted circular cylinder can be described as

$$m_i \ddot{x}_i + c_i \dot{x}_i + K_i x_i = F_i \quad (3)$$

where  $x_1 = x$  and  $x_2 = y$  are the cylinder displacements in the  $x$ - and  $y$ -directions, respectively.  $m_i$ ,  $c_i$ ,  $K_i$  and  $F_i$  are the mass, damping coefficient, structural stiffness and hydrodynamic force in the  $x_i$ -direction, respectively. In this study, the mass is assumed to be identical in the in-line and cross-flow directions, i.e.,  $m_1 = m_2 = m$  and the damping coefficients in the in-line and cross-flow directions are set to zero. Eq. (3) is integrated by using a Newmark integration scheme with a second-order accuracy (Hughes, 1987). The method relates displacements, velocities and accelerations from time step  $n$  to  $n + 1$ :

$$\dot{x}_i^{n+1} = \dot{x}_i^n + \Delta t [(1 - \gamma) \ddot{x}_i^n + \gamma \ddot{x}_i^{n+1}] \quad (4)$$

$$x_i^{n+1} = x_i^n + \Delta t \dot{x}_i^n + \frac{\Delta t^2}{2} [(1 - 2\beta) \ddot{x}_i^n + 2\beta \ddot{x}_i^{n+1}] \quad (5)$$

where  $x_i$  is the displacement in the  $x_i$ -direction, a dot denotes differentiation with respect to time and the superscripts represent the corresponding time step.  $\Delta t$  is the time-step size.  $\beta$  and  $\gamma$  are two real parameters which are directly linked to the accuracy and stability of the scheme. In the present simulation,  $\beta = 1/4$  and  $\gamma = 1/2$  are chosen. The choice of the parameters corresponds to a trapezoidal rule with a second-order accuracy and unconditional stability.

Eqs. (4) and (5) can be rewritten as

$$\ddot{x}_i^{n+1} = \frac{1}{\beta \Delta t^2} (x_i^{n+1} - x_i^n) - \frac{1}{\beta \Delta t} \dot{x}_i^n - \left(1 - \frac{1}{2\beta}\right) \ddot{x}_i^n \quad (6)$$

$$\dot{x}_i^{n+1} = \frac{\gamma}{\beta \Delta t} (x_i^{n+1} - x_i^n) - \left(\frac{\gamma}{\beta} - 1\right) \dot{x}_i^n - \left(\frac{\gamma}{2\beta} - 1\right) \Delta t \ddot{x}_i^n. \quad (7)$$

The displacement in the  $x_i$ -direction at time step  $n + 1$  can be expressed as

$$x_i^{n+1} = \frac{F_i + m_i \left[ \frac{1}{\beta \Delta t^2} x_i^n + \frac{1}{\gamma \Delta t} \dot{x}_i^n + \left(1 - \frac{1}{2\beta}\right) \ddot{x}_i^n \right] + c_i \left[ \frac{\gamma}{\beta \Delta t} x_i^n + \left(\frac{\gamma}{\beta} - 1\right) \dot{x}_i^n + \left(\frac{\gamma}{2\beta} - 1\right) \Delta t \ddot{x}_i^n \right]}{\left(\frac{1}{\beta \Delta t^2} m_i + \frac{\gamma}{\beta \Delta t} c_i + K_i\right)}. \quad (8)$$

### 2.3. Mesh deformation

To accommodate the motion of the cylinder, the displacement diffusion model (Wang and Xiao, 2016; Zhao and Cheng, 2011) for mesh motion is adopted. The displacements of the mesh points are calculated based on the following equation:

$$\nabla \cdot (\Gamma \nabla S_i) = 0 \quad (9)$$

where  $S_i$  represents the displacements of the nodal points in the  $x_i$ -direction,  $\Gamma$  is the mesh stiffness. Our previous numerical simulation (Wang and Xiao, 2016) showed that  $\Gamma = 1/v^2$  with  $v$  being the control volume size could lead to satisfactory results.

### 2.4. Fluid–structure interaction

This classical fluid–structure interaction problem can be solved using a staggered algorithm, i.e., the flow field and the dynamic response of the structure are solved successively at a given time step (Placzek et al., 2009). The simulation within each time step is initiated by solving the Navier–Stokes equations to obtain the forces on the cylinder. Then the forces are transferred to the structural dynamic model to obtain the displacements of the cylinder. The new mesh configuration is evaluated based on the displacements of the cylinder using Eq. (9) and the Navier–Stokes equations are solved on the new mesh configuration. Such a fluid–structure interaction loop is repeated during each time step of the simulation.

## 3. Problem descriptions

### 3.1. Simulation parameters

In the present study, 3D numerical simulation is conducted for an elastically mounted circular cylinder with diameter  $D$  and length  $L$ . The Reynolds number is defined as  $Re = VD/\nu$  and a constant Reynolds number  $Re = 500$  is adopted in the simulation. The choice of  $Re$  stems from several important considerations. First, at  $Re = 500$ , the flow around the cylinder is 3D and it can be modelled by directly solving the 3D Navier–Stokes equations with affordable computational efforts which also avoids the potential uncertainties that might be introduced by the utilisation of turbulence models. Second, the flow structures at low  $Re$  are more regular than those at high  $Re$  which is good for analysing the detailed wake structures and the three-dimensionality of the flow. More importantly, previous studies by Bao et al. (2012) and Leontini et al. (2006) revealed that VIV of rigid structures at low  $Re$  share comparable response features to that at high  $Re$ . Studies on 2DOF VIV at low  $Re$  are also of fundamental research interest from a flow physics point of view.

Batcho and Karniadakis (1991) studied the flow past a circular cylinder at  $Re = 500$  with length-to-diameter ratios ( $L/D$ ) of  $\pi$  and  $2\pi$  and obtained sufficiently accurate results of the force coefficients. The  $L/D = 8$  and  $12$  were used in the 3D simulation of the flow around two circular cylinders in tandem at  $Re \leq 500$  by Carmo et al. (2010); in the present study, the  $L/D$  is also set to  $12$ . It is expected that this spanwise length is large enough to capture the three-dimensionality of the flow at  $Re = 500$ . Furthermore, this  $L/D$  is also comparable to those used in some recent experimental studies on VIV of an elastically mounted circular cylinder (Jauvtis and Williamson, 2004; Kang and Jia, 2013; Sanchis et al., 2008; Srinil et al., 2013; Stappenbelt et al., 2007).

The cylinder is free to vibrate in both the in-line and cross-flow directions. The mass ratios of the cylinder in the in-line and cross-flow directions are set to be identical and take the value of  $m_x^* = m_y^* = m^* = 2$ . Such a low mass ratio is selected because a dramatic change in the fluid–structure interactions of 2DOF VIV was observed by Jauvtis and Williamson (2004) when the mass ratio  $m^*$  is less than  $6$ . The mass ratios in the in-line and cross-flow directions are set to be identical as this scenario is of more practical relevance to real cylindrical offshore structures (Srinil et al., 2013). As the vibration amplitudes reported in previous CFD simulations at low  $Re$  (Bao et al., 2012; Gsell et al., 2016; Lucor and Triantafyllou, 2008; Singh and Mittal, 2005) are smaller than the amplitudes observed in experiments at higher  $Re$  (Blevins and Coughran, 2009; Dahl et al., 2006; Jauvtis and Williamson, 2004; Srinil et al., 2013), in order to maximise the vortex-induced response of

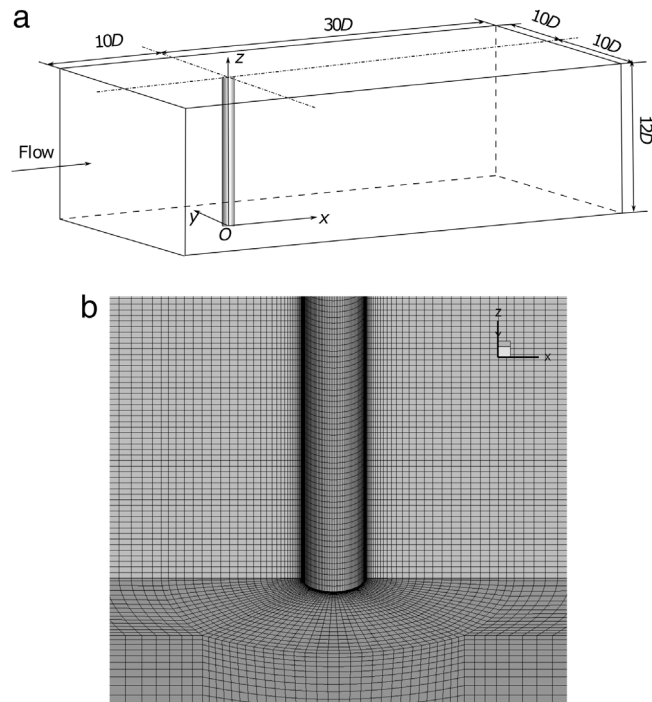


Fig. 1. (a) Computational domain and (b) computational mesh.

the cylinder, the damping coefficients are set to zero by the various authors in their numerical simulations. Similarly, zero damping coefficients in the in-line and cross-flow directions are also adopted in the present study, i.e.,  $c_x = c_y = c = 0$ . The  $V_r$  is varied from 2 to 12 with an increment of 1 and for each  $V_r$ , three natural frequency ratios are considered (i.e.,  $f^* = 1, 1.5$ , and 2).

### 3.2. Computational domain and boundary conditions

Fig. 1(a) shows the computational domain that is used in the present simulation. The size of the domain is  $40D \times 20D \times 12D$ . The cylinder is located at  $10D$  downstream of the inlet boundary and the origin of the Cartesian coordinate system is located at the centre of the bottom end of the cylinder. The computational mesh is displayed in Fig. 1(b). There are 120 nodes along the circumference of the cylinder and the minimum mesh size adjoining the cylinder surface in the radial direction is  $0.001D$ . The boundary conditions for the governing equations are as follows. The surface of the cylinder is assumed to be a no-slip wall. The velocity at the inlet boundary is set to be the same as the freestream velocity. At the outflow boundary, the gradients of the fluid velocity in the streamwise direction are set to zero and the pressure at the outflow boundary is assigned a reference value of zero. The free-slip boundary condition with the velocity in the direction normal to the boundary being zero is used on the two transverse boundaries and a periodic boundary condition is imposed on the top and bottom boundaries. At  $t = 0$ , the displacements and velocities of the cylinder are zero ( $x_1 = x_2 = 0$  and  $\dot{x}_1 = \dot{x}_2 = 0$ ).

### 3.3. Validation test

To verify the numerical methods, 2DOF VIV of a circular cylinder with  $m^* = 10$  and  $L/D = 4$  at  $Re = 1000$  is first simulated. For the purpose of making a reasonable comparison with the numerical results for increasing  $V_r$  in Navrose and Mittal (2013), the  $V_r$  in the present validation test is also increased in small steps. Fig. 2(a) and (b) are the comparisons of the root mean square (rms) of the vibration amplitudes against  $V_r$  in the in-line and cross-flow directions, respectively. The results demonstrate good agreement with those of Navrose and Mittal (2013). The maximum rms in-line and cross-flow vibration amplitudes predicted in both studies are  $A_{xrm}/D \approx 0.016$  and  $A_{yrm} \approx 0.5$ , respectively. This test case demonstrates that the present numerical methods are capable of accurately predicting 2DOF VIV response of an elastically mounted circular cylinder at early subcritical Reynolds numbers.

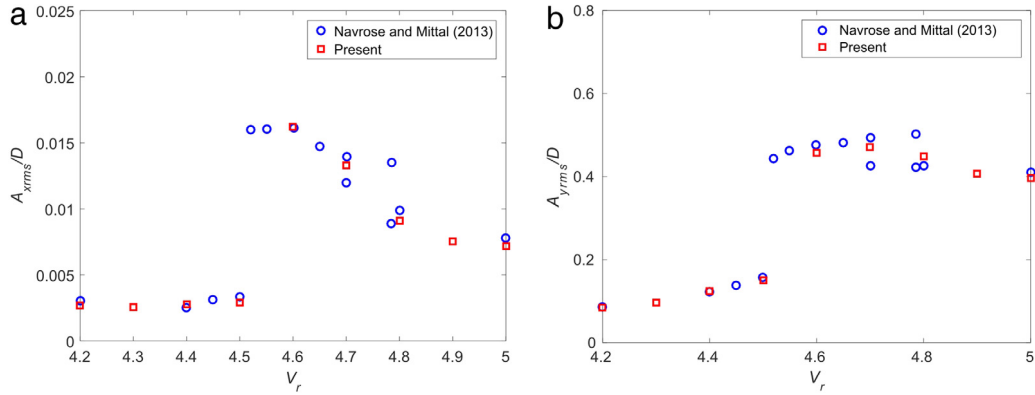


**Fig. 2.** Comparison of the present numerical results with numerical results by Navrose and Mittal (2013) for increasing  $V_r$ : (a) rms of in-line vibration amplitudes and (b) rms of cross-flow vibration amplitudes.

**Table 1**

Comparison of the results from three different meshes.

Mesh	$N_{node}$ (M)	$N_{element}$ (M)	$\Delta z/D$	$\Delta r/D$	$N_c$	$A_x/D$	$A_y/D$	$f_{ox}$	$f_{oy}$	$\theta$ (deg)
1	0.37	0.39	0.2	0.002	96	0.408	0.818	1.875	0.937	341.140
2	0.89	0.93	0.1	0.001	120	0.355	0.797	1.875	0.937	343.540
3	2.27	2.34	0.05	0.001	160	0.341	0.786	1.875	0.937	344.300

**Table 2**

Comparison of the results using different time-step sizes.

$V\Delta t/D$	$A_x/D$	$A_y/D$	$f_{ox}$	$f_{oy}$	$\theta$ (deg)
0.005	0.368	0.819	1.875	0.937	342.560
0.002	0.355	0.797	1.875	0.937	343.540
0.001	0.350	0.808	1.875	0.937	343.870

### 3.4. Mesh dependency study

In order to quantify the dependency of the numerical results on the mesh density, numerical simulation of 2DOF VIV of a circular cylinder at  $f^* = 2$  and  $V_r = 6$  is performed using three different meshes as summarised in Table 1 in which  $N_{node}$ ,  $N_{element}$ ,  $\Delta z$ ,  $\Delta r$  and  $N_c$  represent the number of nodes, the number of elements, the mesh size in the spanwise direction, the minimum mesh size next to the cylinder surface in radial direction and the number of nodes along the circumference of the cylinder, respectively. Quantitative comparisons of the dimensionless oscillation amplitudes ( $A_x/D$ ,  $A_y/D$ ), normalised oscillation frequencies ( $f_{ox}/f_{ny}$ ,  $f_{oy}/f_{ny}$ ) and phase differences ( $\theta$ ) between the nondimensional in-line and cross-flow displacements ( $x/D$  and  $y/D$ ) calculated from the different meshes are provided in Table 1. As is observed in Table 1,  $f_{ox}/f_{ny}$  and  $f_{oy}/f_{ny}$  predicted by the three meshes are identical. The differences in  $A_y/D$  and  $\theta$  between Mesh 2 and Mesh 3 are 1.4% and 0.2%, respectively. The maximum difference of 4.1% occurs in  $A_x/D$  between Mesh 2 and Mesh 3. The comparison among the results from the different meshes suggests that the mesh density of Mesh 2 is sufficient for predicting accurate results of 2DOF VIV at  $Re = 500$ .

### 3.5. Time-step size dependency test

A time-step size dependency test is conducted on Mesh 2 with three nondimensional time-step sizes ( $V\Delta t/D = 0.005$ , 0.002 and 0.001) for the same case as used in the mesh dependency study. The corresponding results are tabulated in Table 2. It shows that the maximum difference between  $V\Delta t/D = 0.005$  and 0.002 is around 3.6% and it decreases to approximately 1.5% between  $V\Delta t/D = 0.002$  and 0.001. Therefore, the numerical results are independent on the time-step size when  $V\Delta t/D \leq 0.002$ . In the consideration of computational efforts,  $V\Delta t/D = 0.002$  is adopted for the simulation in this paper.

## 4. Results and discussions

The 2DOF VIV of a circular cylinder with  $f^* = 1, 1.5$  and 2 at  $Re = 500$  is simulated in a  $V_r$  range of  $V_r = 2-12$ . The effect of  $f^*$  on the 2DOF VIV responses and the 3D flow features around the cylinder is examined.

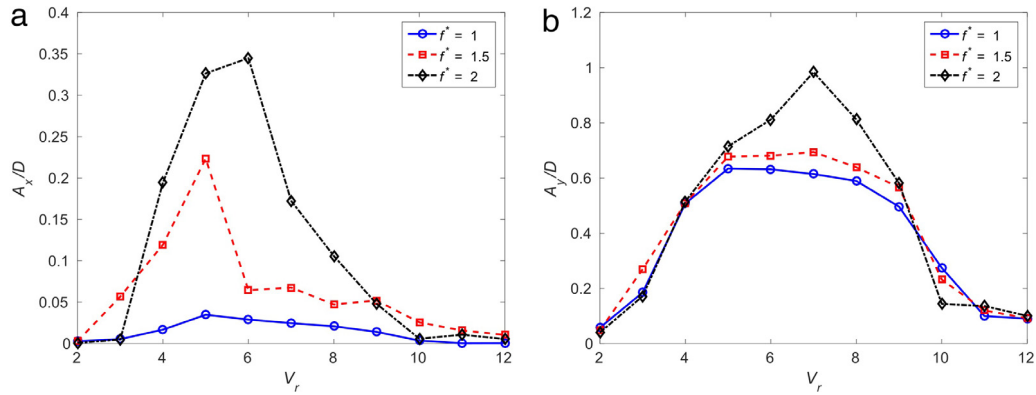


**Fig. 3.** Variation of the response amplitudes with the reduced velocity at different natural frequency ratios: (a) in-line response amplitudes and (b) cross-flow response amplitudes.

#### 4.1. Response amplitudes

Previous studies have shown that  $f^*$  has a significant influence on the vibration amplitudes of the cylinder especially when  $f^*$  is close to 2 (Bao et al., 2012; Dahl et al., 2006; Lucor and Triantafyllou, 2008; Sarpkaya, 1995). In this section, the effect of  $f^*$  on the response amplitudes is explicated. Fig. 3 shows the variation of  $A_x/D$  and  $A_y/D$  with  $V_r$  at different  $f^*$ . As is observed in Fig. 3(a), the maximum in-line amplitude ( $A_{xm}/D$ ) increases in coordination with  $f^*$ .  $A_{xm}/D$  of  $f^* = 1$  and 1.5 appear at an identical reduced velocity  $V_r = 5$  and take the values of  $A_{xm}/D = 0.035$  and 0.224, respectively. When  $f^*$  increases to 2,  $A_{xm}/D$  increases to 0.345 and shifts to a higher reduced velocity  $V_r = 6$ . As for  $A_y/D$ , the amplitude curves of  $f^* = 1$  and 1.5 exhibit similar trends against  $V_r$  with a slight increase in  $A_{ym}/D$  from 0.634 to 0.695 when  $f^*$  increases from 1 to 1.5. A sharp increase in  $A_y/D$  is observable when  $f^*$  increases to 2. Similar to  $A_{xm}/D$ ,  $A_{ym}/D$  also shifts to a higher reduced velocity  $V_r = 7$  and its value increases to  $A_{ym}/D \approx 1$ . The increase of the vibration amplitude ( $A/D$ ) and the shift of the peak amplitude ( $A_m/D$ ) to a higher reduced velocity when  $f^*$  varies from 1 to 2 were also observed in the 2D numerical simulation of Lucor and Triantafyllou (2008) at  $Re = 1000$  and Bao et al. (2012) at  $Re = 150$ .

The shapes of the response curves in the present study are qualitatively similar to those obtained from the 2D CFD simulation at  $Re = 150$  by Bao et al. (2012) (Fig. 4). The lock-in ranges of the present results are wider than those in Bao et al. (2012) owing to the lower  $m^*$  used in the present simulation. When  $f^* = 2$ , multiple small peaks were observed by Bao et al. (2012) whereas the cross-flow response at  $f^* = 2$  in the present simulation shows a single peak. In order to investigate the possible explanations for this discrepancy, a 2D simulation of 2DOF VIV of a circular cylinder with the same parameters as in the study of Bao et al. (2012) is conducted at  $f^* = 2$  and the results are plotted in Fig. 4(c). As is shown in Fig. 4(c), the cross-flow response in the present 2D simulation also displays a single peak. It is thus speculated that the discrepancy can be attributed to the variance in the stability of the numerical methods used for solving the structural dynamic equations. In fact, Bao et al. (2012) used an explicit time integration method which is conditionally stable while the Newmark integration scheme used in the present study is unconditionally stable.

With  $m_x^* \neq m_y^*$ , Sarpkaya (1995) and Dahl et al. (2006) observed a two-peak cross-flow response when  $f^*$  approaches 2. However, the studies of Lucor and Triantafyllou (2008) and Srinil et al. (2013) with  $m_x^* = m_y^*$  revealed a single-peak cross-flow response. Srinil et al. (2013) attributed the single-peak cross-flow response at  $f^* \approx 2$  to  $m_x^* = m_y^*$ . The observation of the single-peak cross-flow responses in the present 2D and 3D simulations when  $f^* = 2$  for  $m_x^* = m_y^*$  is consistent with the conclusion by Srinil et al. (2013).

As noted above, in the present 3D simulation,  $A/D$  increases and  $A_m/D$  shifts to a higher  $V_r$  when  $f^*$  increases from 1 to 2, which is consistent with the numerical simulation results by Lucor and Triantafyllou (2008) at  $Re = 1000$  and Bao et al. (2012) at  $Re = 150$ . Conversely, the change in  $A/D$  as well as the shift of  $A_m/D$  when  $f^*$  varies from 1 to 2 in the experimental studies by Dahl et al. (2006) ( $Re = 11,000$ – $60,000$ ) and Srinil et al. (2013) ( $Re = 2,000$ – $50,000$ ) at higher  $Re$  are not obvious. Furthermore, compared to  $A_{ym}/D$  of around 1.5 in the experimental studies, the present  $A_{ym}/D$  is relatively small. The aforementioned differences in the amplitude responses indicate the possible influence of  $Re$  on 2DOF VIV as suggested by Swithenbank et al. (2008).

#### 4.2. Response frequencies

The occurrence of dual resonance has been widely reported for 2DOF VIV (Bao et al., 2012; Dahl et al., 2010; Srinil and Zanganeh, 2012; Srinil et al., 2013; Wang and Xiao, 2016; Zanganeh and Srinil, 2014). Fig. 5 shows the variation of  $f_{ox}/f_{ny}$  and  $f_{oy}/f_{ny}$  with  $V_r$  at different  $f^*$ . According to the synchronisation between the response frequency and the natural frequency

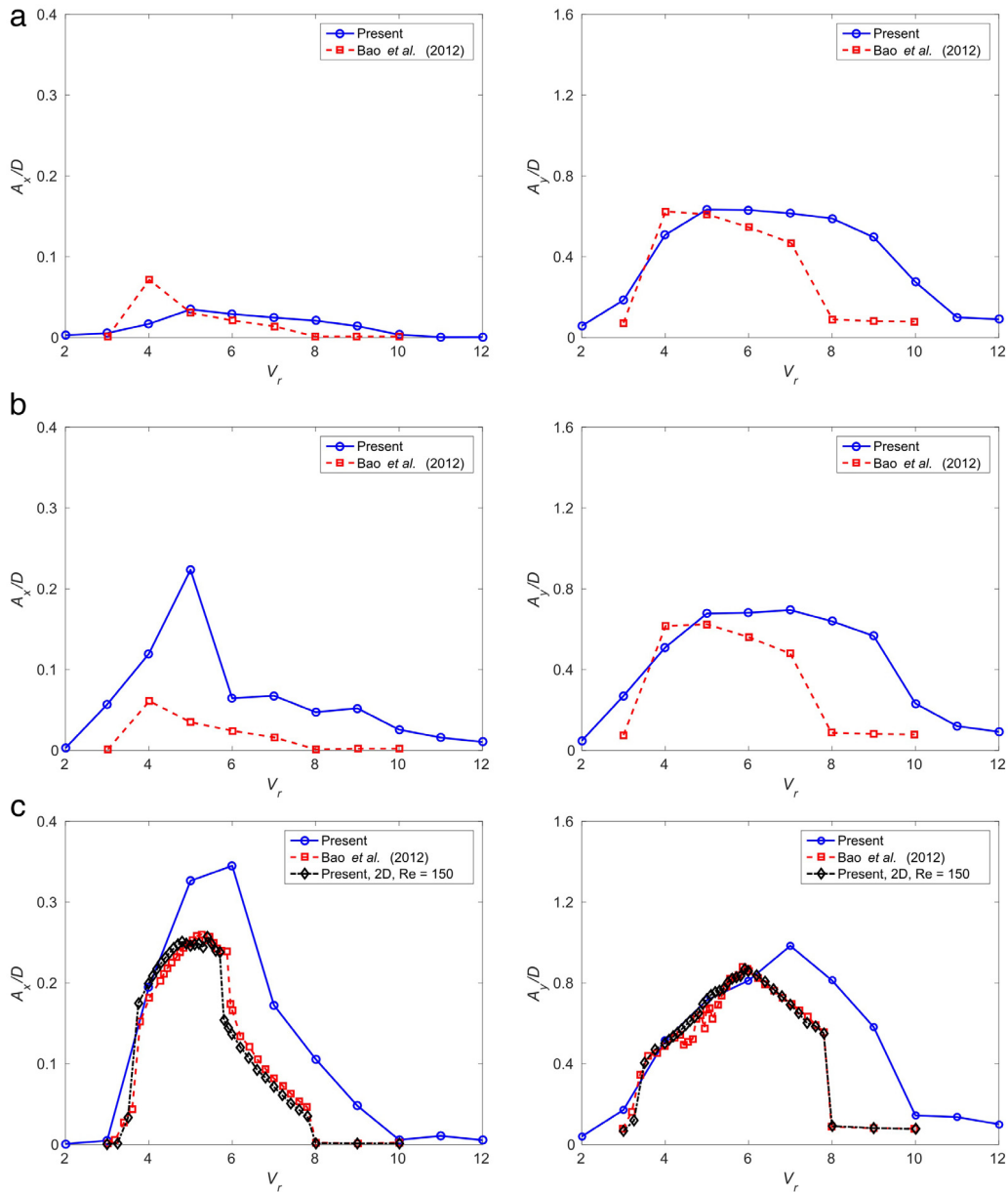
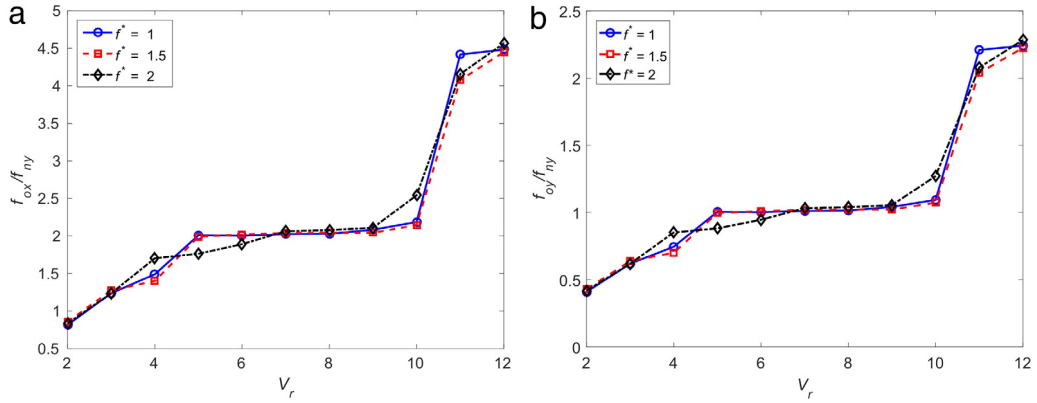


Fig. 4. Comparison of amplitude response curves between the present simulation and Bao et al. (2012): (a)  $f^* = 1$ , (b)  $f^* = 1.5$  and (c)  $f^* = 2$ .

in Fig. 5, the lock-in ranges of the three different  $f^*$  are identical, i.e.,  $V_r = 5-10$ .  $f_{ox}/f_{ny}$  and  $f_{oy}/f_{ny}$  are almost constant within the lock-in range and are linear functions of  $V_r$  in the pre-lock-in ( $2 \leq V_r < 5$ ) and post-lock-in ( $10 < V_r \leq 12$ ) ranges. It can also be understood from Fig. 5 that the ratio of the in-line oscillation frequency to the cross-flow oscillation frequency is around 2 regardless of  $f^*$ . As is explained by Dahl et al. (2010), under dual resonance, the cylinder vibrates at frequencies approaching the Strouhal frequency  $f_v$  in the transverse direction and  $2f_v$  in the in-line direction, respectively. The 2:1  $f_{ox}/f_{oy}$  in the present study indicates that dual resonance exists over a wide range of the natural frequency ratios.

The time histories of the total drag coefficient  $C_D = F_x/(0.5\rho V^2 DL)$ , total lift coefficient  $C_L = F_y/(0.5\rho V^2 DL)$ ,  $x/D$  and  $y/D$  at  $V_r = 3$  and 6 when  $f^* = 1$  are illustrated in Fig. 6, which reveal the vibrations are regular at  $V_r = 6$  as compared to  $V_r = 3$  where the beating phenomenon occurs. The beating behaviour in the pre-lock-in range agrees with the observations of Navrose and Mittal (2013) and Zhao et al. (2014). Zhao et al. (2014) attributed the beating phenomenon to the 2D feature of the flow. The present study confirms the strong two-dimensionality of the flow at low reduced velocities by investigating the correlation lengths and vortex structures in Sections 4.6 and 4.7, respectively.



**Fig. 5.** Variation of the response frequencies with the reduced velocity at different natural frequency ratios: (a) in-line response frequencies and (b) cross-flow response frequencies.

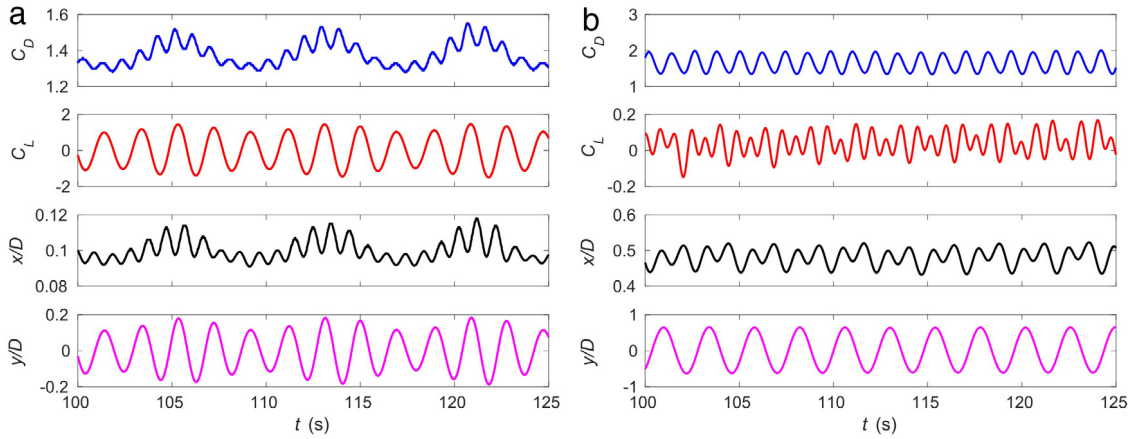


**Fig. 6.** Time histories of the cylinder displacements and total lift and drag coefficients when  $f^* = 1$ : (a)  $V_r = 3$  and (b)  $V_r = 6$ .

### 4.3. Orbital trajectories

Dahl et al. (2008) reported that the orbital shape of the cylinder is critical in defining the amplitude and frequency content of the hydrodynamic forces and according to Bourguet et al. (2013), the direction of the orbital motion is closely related to the energy transfer between the fluid and the structure. Therefore, it is of great significance to study the effect of  $f^*$  on the orbital trajectories of the cylinder. The variation of the orbital trajectories with  $V_r$  at different  $f^*$  is displayed in Fig. 7(a). It can be observed that most of the orbital trajectories are of a figure-eight shape which is indicative of the 2:1  $f_{ox}/f_{oy}$ . Thus, the figure-eight trajectories are also evidence of the occurrence of dual resonance (Dahl et al., 2010).

The orbit orientation of a trajectory is related to the phase difference ( $\theta$ ) between  $x/D$  and  $y/D$ . As elucidated by Huera-Huarte and Bearman (2009) and Bourguet et al. (2013), the phase difference can be defined as  $\theta = \theta_x - 2\theta_y$ , where  $\theta_x$  and  $\theta_y$  are phase angles of the in-line and cross-flow responses. According to Jauvtis and Williamson (2004), an orbital trajectory is counterclockwise when  $0^\circ \leq \theta < 90^\circ$  or  $270^\circ < \theta \leq 360^\circ$  and clockwise when  $90^\circ < \theta < 270^\circ$ . Crescent shapes correspond to  $\theta = 90^\circ$  or  $270^\circ$ . The phase differences demonstrated in Fig. 7(b) highlight that most of the orbital trajectories are counterclockwise, i.e., the cylinder motion is counterclockwise at the top of the figure-eight motion. The exceptional clockwise trajectories are highlighted in red in Fig. 7(a) and a close-up of the orbital trajectory at  $V_r = 3$  and  $f^* = 1.5$  is displayed in Fig. 8(a) revealing that the trajectory is of a clockwise figure-eight shape.

As determinable from Fig. 7(a), the number of clockwise trajectories decreases as  $f^*$  increases from 1 to 2. The counterclockwise direction is the predominant orbit orientation in the lock-in range. The observation agrees with that reported by Bourguet et al. (2011). According to Dahl et al. (2007), the upstream motion of the cylinder in a counterclockwise trajectory leads to a closer proximity of the cylinder and the recently shed vortices and energy is transferred from the fluid to the body. Whereas in clockwise orbits, the flow acts as the damping of the cylinder vibration (Bourguet et al., 2011). Oblique figure-eight trajectories similar to those reported by Kang and Jia (2013) and Gedikli and Dahl (2014) are observed at  $V_r = 6, 7$  and  $8$  when  $f^* = 1$  in the present study. Fig. 8(b) illustrates the oblique figure-eight trajectory at  $V_r = 6$  and

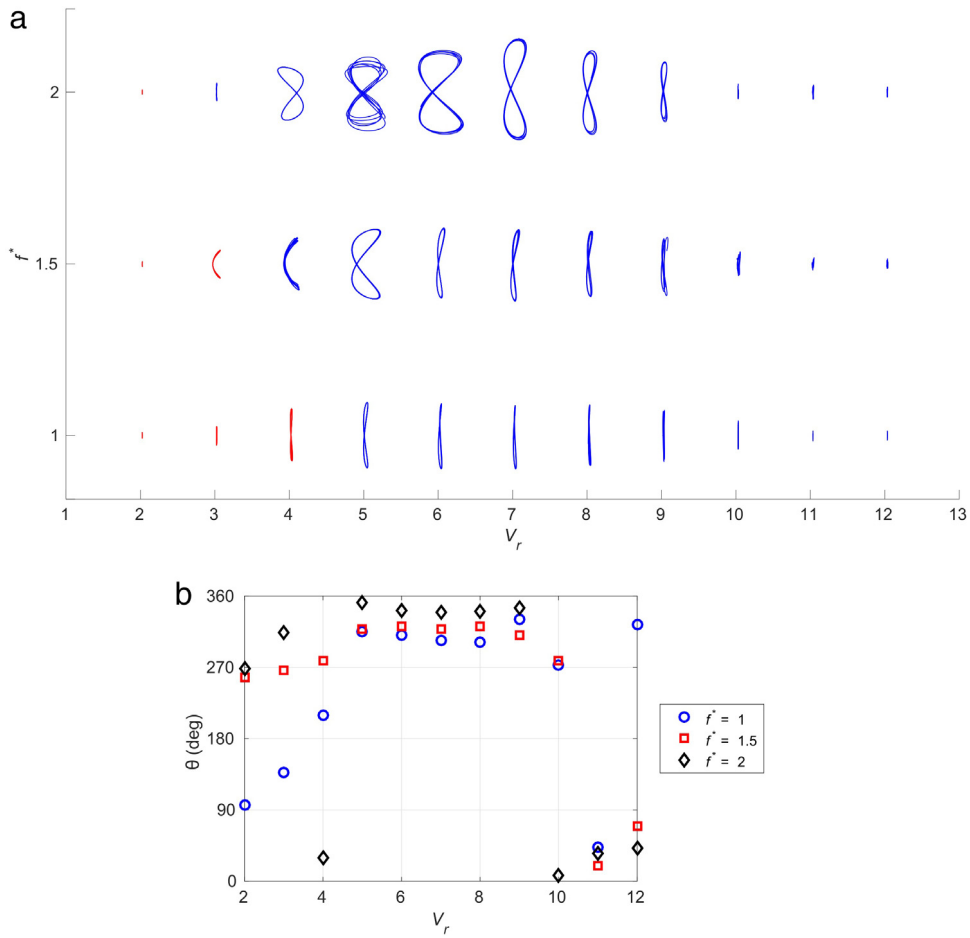


**Fig. 7.** (a) Variation of the orbital trajectories with the reduced velocity at different natural frequency ratios and (b) variation of the phase differences between in-line and cross-flow displacements with the reduced velocity at different natural frequency ratios. (For interpretation of the references to colour in this figure legend, the reader is referred to the web version of this article.)

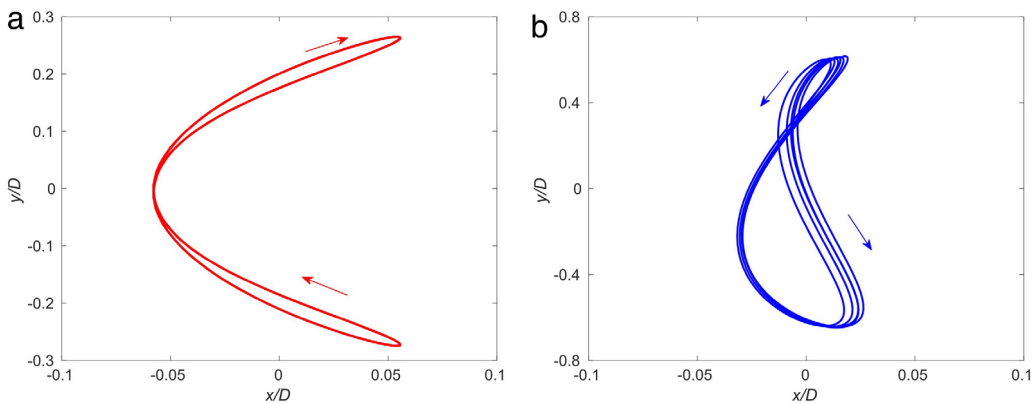


**Fig. 8.** Zoom-in view of orbital trajectories: (a) clockwise figure-eight trajectory at  $V_r = 3$  and  $f^* = 1.5$  and (b) oblique counterclockwise figure-eight trajectory at  $V_r = 6$  and  $f^* = 1$ .

$f^* = 1$ . The amplitude spectra of  $x/D$  and  $y/D$  at  $V_r = 6$  and  $f^* = 1$  are plotted in Fig. 9. Similar to other cases under dual resonance, the ratio of the dominant in-line to cross-flow oscillation frequencies in an oblique figure-eight trajectory is also approximately 2. However, for the in-line displacement, apart from the dominant frequency component at twice

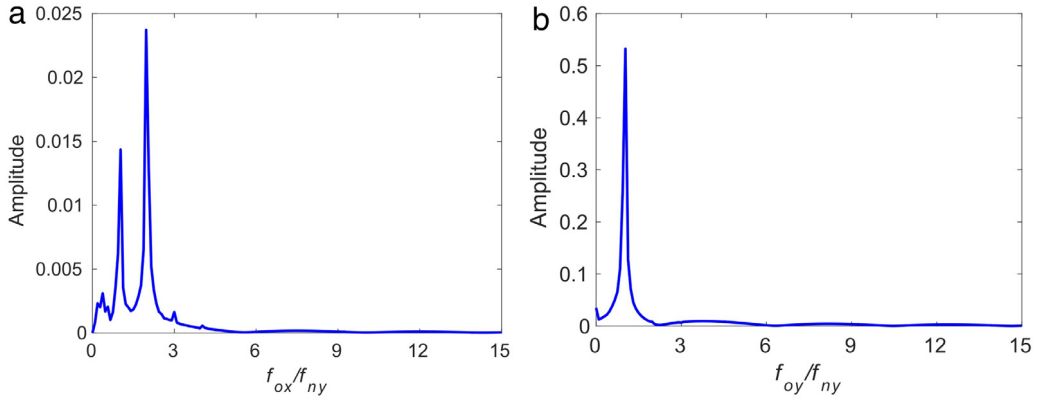


**Fig. 9.** Amplitude spectra of displacements at  $V_r = 6$  and  $f^* = 1$ : (a) in-line displacement and (b) cross-flow displacement.

the cross-flow oscillation frequency ( $2f_{oy}$ ), there is also a frequency component equal to  $1f_{oy}$ . The additional  $1f_{oy}$  frequency component in  $x/D$  leads to the asymmetry of the Lissajous figure.

#### 4.4. Hydrodynamic forces

When the cylinder is vibrating in two degrees of freedom, the in-line vibration has significant influence on the hydrodynamic forces. Fig. 10 shows the variation of  $C_D$  and  $C_L$  with  $V_r$ . As is observed in Fig. 10(a), the mean drag coefficient ( $C_{Dmean}$ ) curves of  $f^* = 1$  and 1.5 nearly coincide, while an obvious increase in the  $C_{Dmean}$  is observed at  $f^* = 2$ . The rms values of the oscillating drag coefficient ( $C_{Drms}$ ) jump notably at  $f^* = 2$  and  $V_r = 4$ . The peak  $C_{Drms}$  is nearly three times as large as it is at  $f^* = 1$  and 1.5. The large drag fluctuation agrees with the observations of Dahl et al. (2010) and Bao et al. (2012). Compared to the oscillating drag, the fluctuation of the rms values of the oscillating lift coefficient ( $C_{Lrms}$ ) is less sensitive to  $f^*$ .

The time histories of  $C_D$  and  $C_L$  at  $V_r = 3$  and 6 when  $f^* = 1$  are shown in Fig. 6. Similar to the VIV responses, the beating phenomenon is also discernible in the hydrodynamic force coefficients at  $V_r = 3$  which again can be attributed to the 2D feature of the flow at low reduced velocities. The  $C_L$  time history makes evident that there is a third harmonic component in  $C_L$  at  $V_r = 6$ . Fig. 11 shows the amplitude spectra of  $C_L$  at different  $f^*$ . It is apparent that for the three  $f^*$  considered in the present study, there is a third harmonic component in  $C_L$  in the lock-in range. The third harmonic forces were found to be associated with the counterclockwise motion of the cylinder by Dahl et al. (2010). With the increase of the natural frequency ratio, the third harmonic component becomes larger.

#### 4.5. Effective added mass coefficients

It is observed in Fig. 5 that  $f_{ox}/f_{oy}$  is always in the vicinity of 2 regardless of  $f^*$ . The 2:1  $f_{ox}/f_{oy}$  at different  $f^*$  is the consequence of the change in the effective added mass. According to Dahl et al. (2010), the oscillation frequency of the cylinder can be defined as follows.

$$f_o = \sqrt{\frac{K}{m + m_{ea}}} \quad (10)$$

where  $m_{ea}$  is the effective added mass. The effective fluid added mass force changes  $m_{ea}$  of the system leading to the 2:1  $f_{ox}/f_{oy}$ , although  $f^*$  may be distant from 2. Similar to the mass ratio  $m^*$ , the effective added mass can be nondimensionalised as  $C_m = m_{ea}/(\rho\pi D^2 L/4)$ . The coefficient  $C_m$  represents a force coefficient due to vortex dynamics that is in phase with the acceleration of the cylinder. The effective added mass coefficients in the in-line and cross-flow directions ( $C_{mx}$  and  $C_{my}$ ) are determined based on the second harmonic component of the fluctuating drag and the first harmonic component of the lift as in Jauvtis and Williamson (2004).

$$C_{mx} = \frac{2V^2 C_{D2} \cos(\phi_x)}{\pi (A_x/D) D^2 (2\pi f_{ox})^2} \quad (11)$$

$$C_{my} = \frac{2V^2 C_{L1} \cos(\phi_y)}{\pi (A_y/D) D^2 (2\pi f_{oy})^2} \quad (12)$$

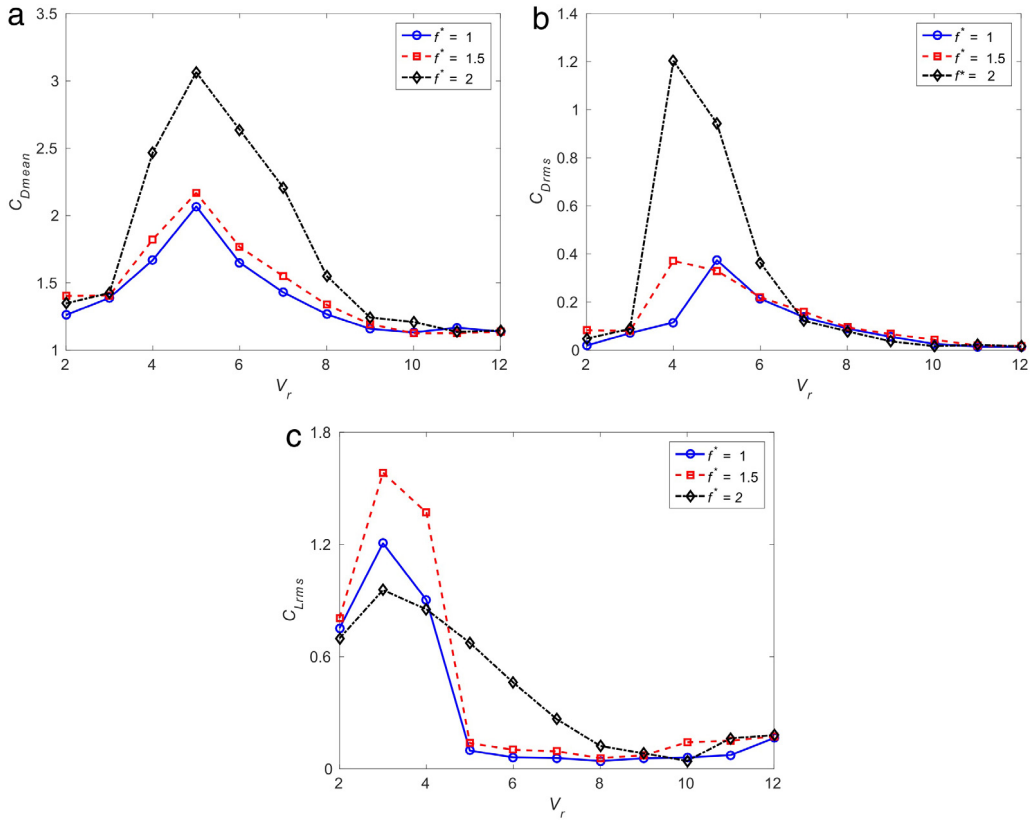


**Fig. 10.** Variation of the hydrodynamic force coefficients with the reduced velocity at different natural frequency ratios: (a) mean drag coefficients, (b) rms of total drag coefficients and (c) rms of total lift coefficients.

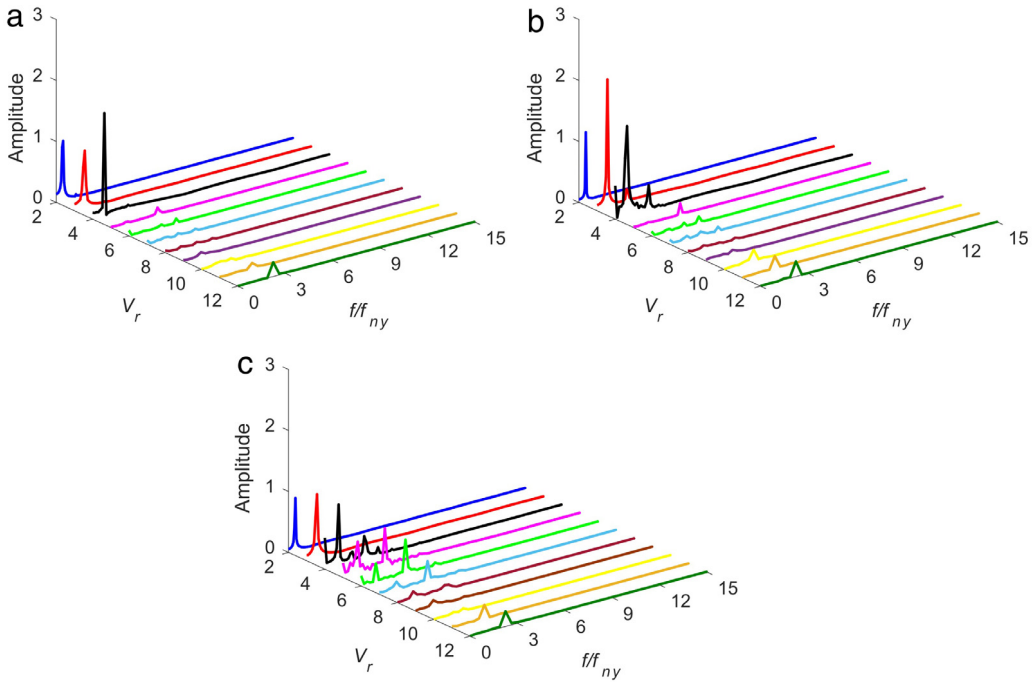


**Fig. 11.** Amplitude spectra of the total lift coefficients: (a)  $f^* = 1$ , (b)  $f^* = 1.5$  and (c)  $f^* = 2$ .

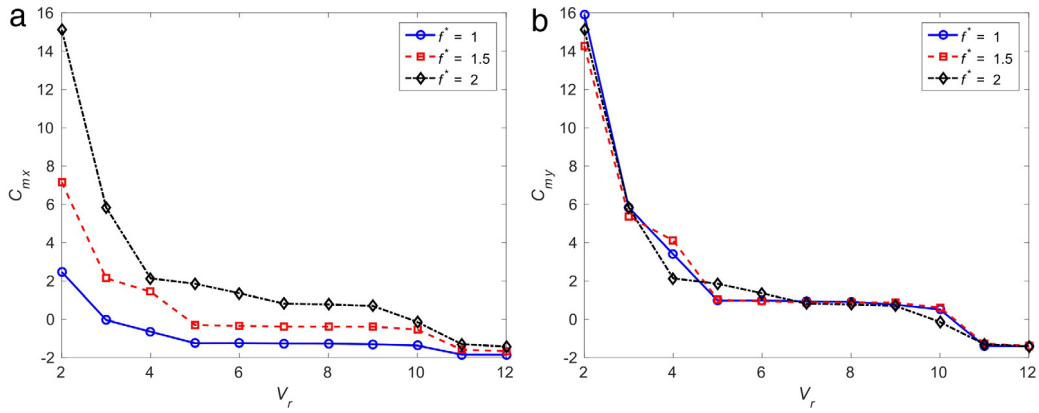


**Fig. 12.** Variation of the effective added mass coefficients with the reduced velocity at different natural frequency ratios: (a) in-line effective added mass coefficients and (b) cross-flow effective added mass coefficients.

where  $C_{D2}$  and  $\phi_x$  are the magnitude of the second harmonic component of the fluctuating drag coefficient and its phase angle with respect to  $x/D$ , respectively.  $C_{L1}$  and  $\phi_y$  are the magnitude of the first harmonic component of  $C_L$  and its phase angle with respect to  $y/D$ , respectively.

Fig. 12 demonstrates the variation of  $C_{mx}$  and  $C_{my}$  with  $V_r$  at different  $f^*$ . According to Fig. 12(a),  $C_{mx}$  decreases with the increase of  $V_r$ . The decreasing trend is observed for all the three  $f^*$  considered and it is also reflected by the increase of  $f_{ox}/f_{ny}$  with the increase of  $V_r$  as shown in Fig. 5. A large deviation is observed for the  $C_{mx}$  curves at different  $f^*$ . At  $f^* = 1$ , most of the  $C_{mx}$  values are negative. By contrast, they become positive throughout the  $V_r$  range considered when  $f^* = 2$ . Negative  $C_{mx}$  with the lowest value being around  $-2$  was also reported by Bao et al. (2012) in their 2D CFD study and in the reduced-order modelling of Zanganeh and Srinil (2014). In the cross-flow direction,  $C_{my}$  also decreases with the increase of  $V_r$ . However, unlike the  $C_{mx}$  curves, the  $C_{my}$  curves at different  $f^*$  show obvious overlap in the range of  $V_r$  considered. This seems reasonable because a larger variation of  $C_{mx}$  is required in order to drive  $f_{ox}/f_{oy}$  to 2 when  $f^*$  is distant from 2.

#### 4.6. Correlation lengths

The three-dimensionality of the flow in the near wake of the cylinder which determines the fluctuations of the forces acting on the cylinder is measured by the spanwise correlation length. Previous experimental and numerical studies indicated that there was a sharp drop in spanwise correlation at the end of the upper branch near the transition between the upper and lower branches, which does not diminish the response of the cylinder (Hover et al., 2004, 1998; Lucor et al., 2003, 2005; Zhao et al., 2014). In the present study, the autocorrelation function defined by Lucor et al. (2005) is used to quantify the correlation. The autocorrelation function is described as follows.

$$R(l, t) = \frac{1}{N_t} \sum_{j=1}^{N_t} \left[ \frac{(1/N_z) \sum_{i=1}^{N_z} C_L(z_i, t_j) C_L(z_i - l_k, t_j)}{(1 - N_z) \sum_{i=1}^{N_z} C_L^2(z_i, t_j)} \right] \quad (13)$$

where  $C_L(z_i, t_j)$  is taken to be the fluctuation of the original signal  $C_L^*(z_i, t_j)$  from which its mean quantity is subtracted. The signal  $C_L(z_i, t_j)$  is given by

$$C_L(z_i, t_j) = C_L^*(z_i, t_j) - \frac{1}{N_t} \sum_{n=1}^{N_t} C_L(z_i, t_n). \quad (14)$$

The shift  $l_k$  in Eq. (13) is prescribed to be

$$l_k = k \times l = k \times dz \text{ with } dz = l/N_z \text{ and } k = \left[ 0, 1, 2, \dots, \frac{N_z}{2} \right]. \quad (15)$$

The correlation length  $L_C$  is then computed by

$$L_C(t) = 2 \int_0^{L/D} R(l, t) dl. \quad (16)$$

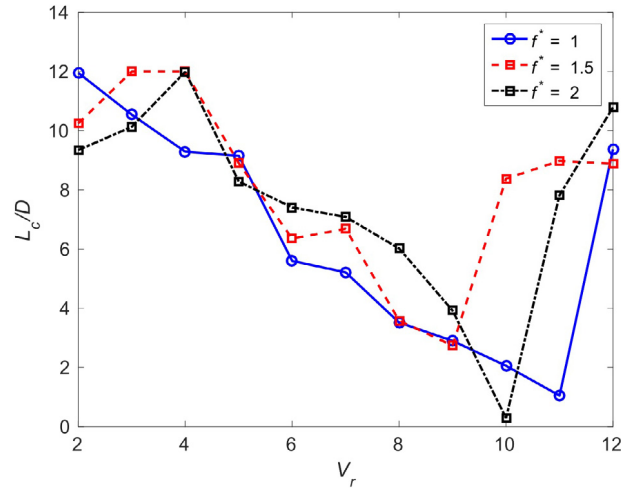


Fig. 13. Variation of the correlation lengths with the reduced velocity at different natural frequency ratios.

Fig. 13 shows the variation of the nondimensional correlation length ( $L_c/D$ ) with  $V_r$  at different  $f^*$ . At  $f^* = 1$ , the maximum correlation length is witnessed at  $V_r = 2$  while it shifts to  $V_r = 4$  when  $f^* = 1.5$  and 2. In general,  $L_c/D$  is very large for low  $V_r$  in the pre-lock-in range which is an indication of the strong two-dimensionality of the flow. As has been alluded to in the previous sections, the strong two-dimensionality of the flow is the cause of the beating phenomenon in the VIV responses and the hydrodynamic forces. There is a drop in  $L_c/D$  as  $V_r$  increases and it reaches its minimum value at  $V_r$  close to the transition region between lock-in and post-lock-in ranges. Finally,  $L_c/D$  increases for larger  $V_r$  in the post-lock-in range.

The variation of  $C_L$  along the span at  $V_r = 3, 6$  and 9 for  $f^* = 1$  and 2 is examined by plotting the contours of the sectional lift coefficient ( $C_L(z) = F_y(z)/(0.5\rho V^2 D)$ ) on the  $z-t$  plane. These three  $V_r$  are selected in a way that  $V_r = 3$  represents the cases with large  $L_c/D$ .  $V_r = 6$  is in proximity to the location where  $A_m/D$  appears and  $V_r = 9$  is near the region where  $L_c/D$  approaches its minimum value. As for the two  $f^*$ ,  $f^* = 1$  and 2 correspond to the most common case of 2DOF VIV and the scenario where perfect 2DOF resonance might occur, respectively. Fig. 14 demonstrates that the  $C_L$  distribution along the span is well organised at  $V_r = 3$  for both  $f^* = 1$  and 2 revealing the 2D feature of the flow at  $V_r = 3$ . When  $V_r$  increases to 6, the variation of  $C_L$  along the span grows stronger.  $C_L(z)$  at different spanwise locations suffer relative phase shifts with each other which consequently results in the variation of the phase difference between  $C_L(z)$  and  $y/D$  along the cylinder. The decrease in  $L_c/D$  can be attributed to the poor phasing between the forces and the displacement (Lucor et al., 2003, 2005). With an increase in  $V_r$  to 9, the relative phase shifts among  $C_L(z)$  signals become more obvious leading to an even poorer correlation. The observation from the contours of  $C_L(z)$  agrees with the conclusion drawn from the computed  $L_c/D$  in Fig. 13.

#### 4.7. Vortex shedding

One of the objectives of this paper is to study the effect of the natural frequency ratio on the vortex shedding of 2DOF VIV. The 3D vortex structures are defined using the  $\lambda_2$  method proposed by Jeong and Hussain (1995) in which  $\lambda_2$  is the second eigenvalue of the symmetric tensor  $\mathbf{S}^2 + \mathbf{\Omega}^2$ . Here,  $\mathbf{S}$  and  $\mathbf{\Omega}$  are the symmetric and antisymmetric parts of the velocity gradient tensor  $\nabla \mathbf{u}$ . Fig. 15 presents the iso-surfaces of  $\lambda_2$  at  $V_r = 3, 6$  and 9 for  $f^* = 1$  and 2. The reasons for the choice of specific combinations of  $V_r$  and  $f^*$  are provided in Section 4.6. The spanwise vorticity defined as  $\omega_z = \partial u_2/\partial x_1 - \partial u_1/\partial x_2$  are plotted on the iso-surfaces. It can be observed that the wake flow is entirely 3D. The wake in the lock-in range is wider than that in the non-lock-in range. Among the three  $V_r$  considered for each  $f^*$ , the widest wake is observed at  $V_r = 6$  which is close to the  $V_r$  where  $A_m/D$  appears. The variation of the flow in the lock-in range is also stronger than in the non-lock-in range. The vortices in the spanwise direction can be clearly identified at  $V_r = 3$  for both  $f^* = 1$  and 2. The clearly identifiable spanwise vortices indicate the strong two-dimensionality of the flow at low  $V_r$  which is related to the beating phenomenon as discussed in Sections 4.2 and 4.4. With the increases of  $V_r$  and  $f^*$ , the variation of the spanwise vortices becomes stronger but they can still be identified at  $V_r = 6$  and  $f^* = 1$ . However, it is difficult to identify the spanwise vortices in the remainder of the cases presented in Fig. 15. The changes in the spanwise vortices agree with the variation of  $L_c/D$  as shown in Fig. 13.

To further examine the variation of the flow in the spanwise direction of the cylinder, the contours of  $\omega_z$  at four instants of time in one cycle ( $t = 0, 0.25T_{oy}, 0.5T_{oy}$  and  $0.75T_{oy}$  where  $T_{oy}$  is the period of the cross-flow vibration) are plotted. The corresponding  $y/D$  at different time instants are: 0,  $A_y/D$ , 0 and  $-A_y/D$ , respectively. At each time instant considered,  $\omega_z$  on three cross sections ( $z/L = 0.25, 0.5$  and  $0.75$ ) are presented to study the variation of the vortex shedding modes along the cylinder. The three cross sections are chosen in favour of those closer to the cylinder ends to avoid the potential end effect of the periodic boundary condition employed on the two spanwise boundaries.

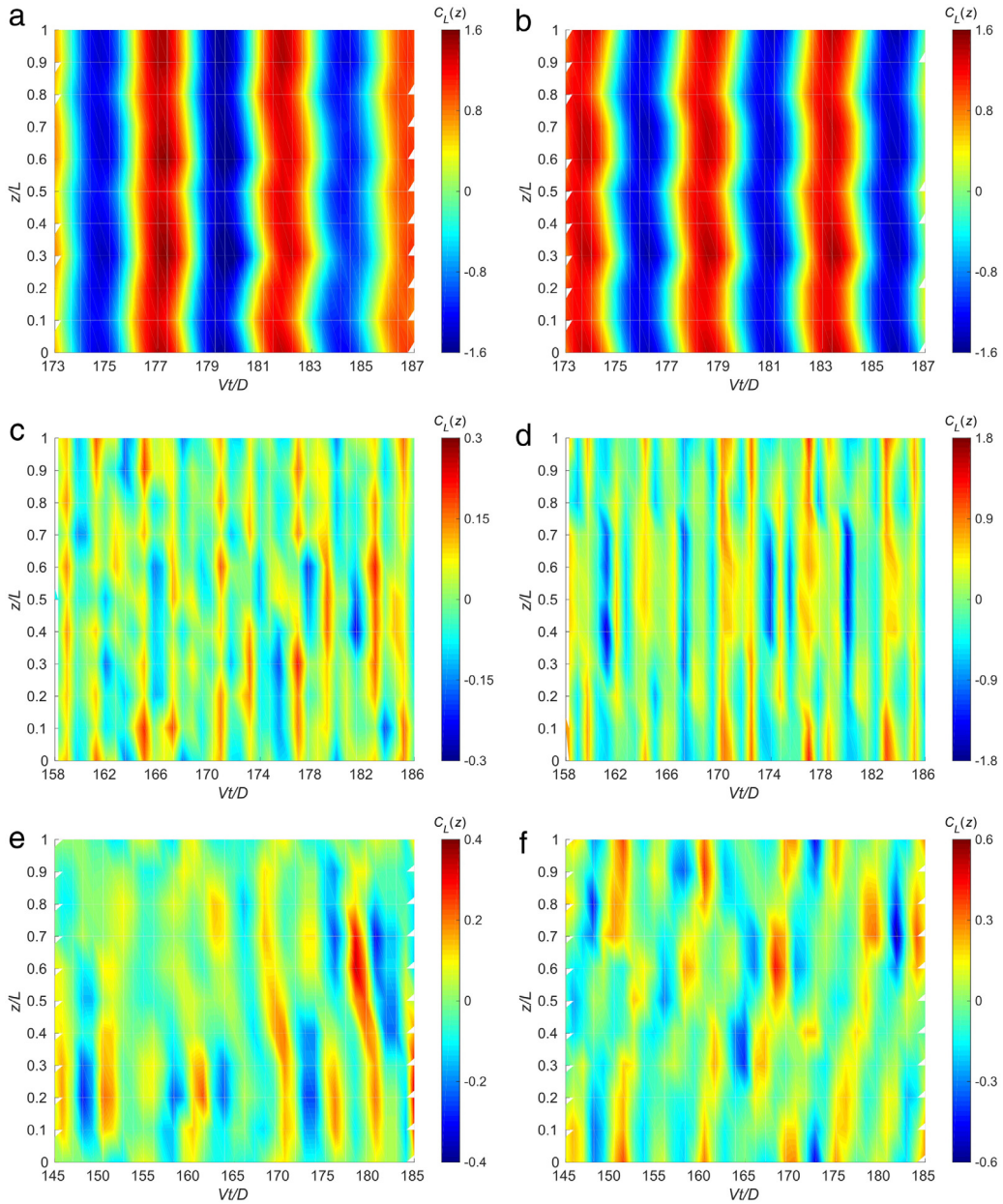


**Fig. 14.** Contours of the sectional lift coefficients: (a)  $V_r = 3$  and  $f^* = 1$ , (b)  $V_r = 3$  and  $f^* = 2$ , (c)  $V_r = 6$  and  $f^* = 1$ , (d)  $V_r = 6$  and  $f^* = 2$ , (e)  $V_r = 9$  and  $f^* = 1$  and (f)  $V_r = 9$  and  $f^* = 2$ .

Figs. 16 and 17 are the  $\omega_z$  contours in one cycle on the three cross sections when  $V_r = 3$  for  $f^* = 1$  and 2. By comparing the vorticity contours at different time instants on each cross section, the vortex shedding in both cases is found to demonstrate a clear 2S pattern with two single vortices being formed in one cycle as described by Williamson and Roshko (1988). The vortex shedding flows on the different cross sections are nearly in phase with each other and the vortex shedding patterns are very similar indicating the strong two-dimensionality of the flow at low  $V_r$  in the pre-lock-in range. Such vortex wake structure leads to the well-organised distribution of  $C_L(z)$  along the cylinder span at  $V_r = 3$ , as mentioned in Section 4.6.

Fig. 18 shows the  $\omega_z$  contours when  $V_r = 6$  and  $f^* = 1$ . As is explicated in Section 4.3, the orbital trajectory of the cylinder in this case is an oblique figure-eight shape. Therefore, it is anticipated that the wake of the cylinder would display asymmetry. It can be seen from Fig. 18 that the vortex shedding at  $z/L = 0.25$  and  $0.5$  exhibits a P + S mode where the cylinder sheds a single vortex and a vortex pair per cycle. The P + S mode was first identified in forced vibration experiments (Griffin and Ramberg, 1974; Zdera et al., 1995) and recently has also been detected in the free vibration studies by Singh

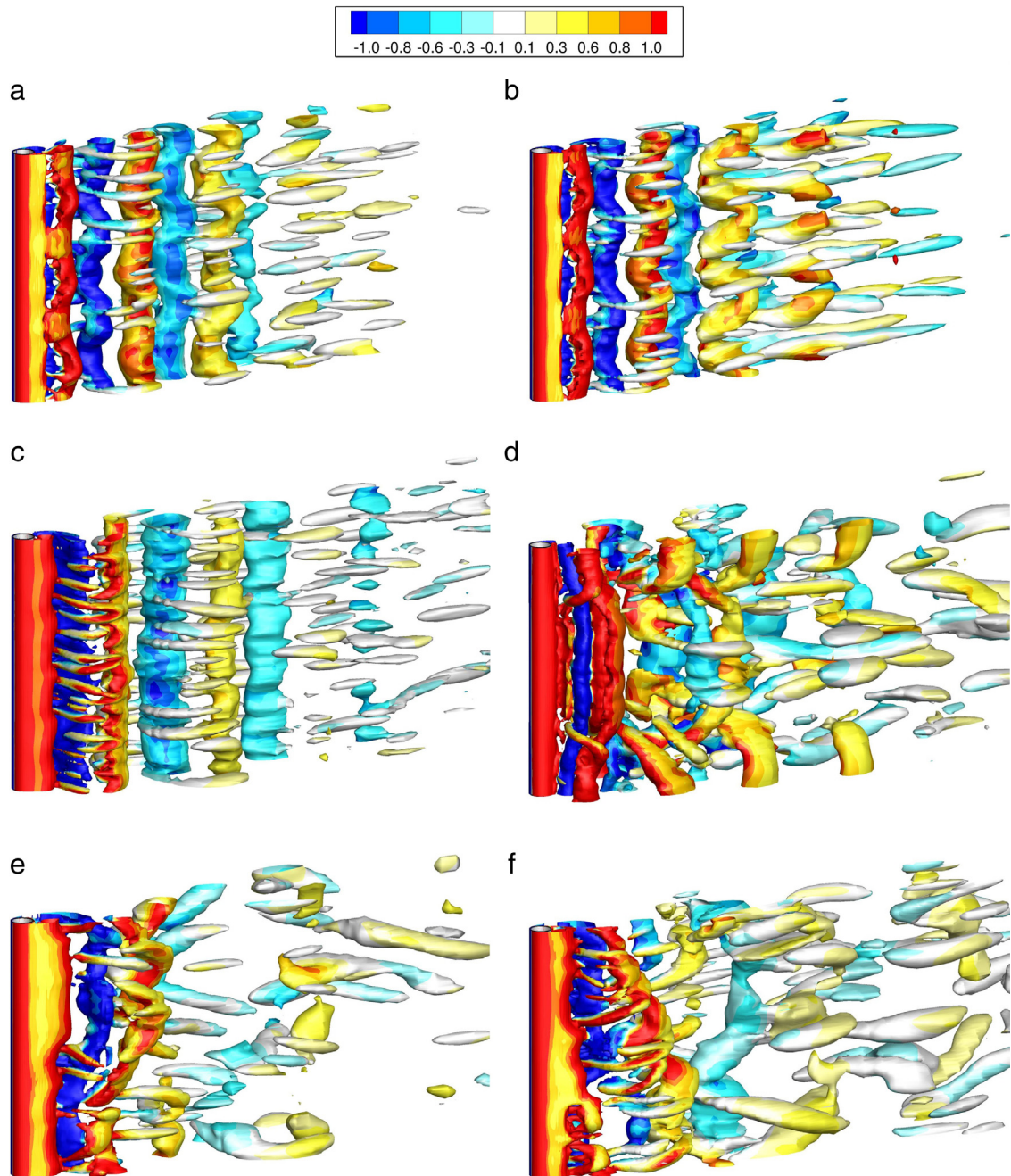


**Fig. 15.** Isosurfaces of eigenvalue  $\lambda_2$  with the contours of the spanwise vorticity  $\omega_z$  on the isosurfaces: (a)  $V_r = 3$  and  $f^* = 1$ , (b)  $V_r = 3$  and  $f^* = 2$ , (c)  $V_r = 6$  and  $f^* = 1$ , (d)  $V_r = 6$  and  $f^* = 2$ , (e)  $V_r = 9$  and  $f^* = 1$  and (f)  $V_r = 9$  and  $f^* = 2$ .

and Mittal (2005), Bao et al. (2012) and Gedikli and Dahl (2014). In spite of the P + S mode at  $z/L = 0.25$  and  $0.5$ , a 2S mode appears at  $z/L = 0.75$ . The dominant asymmetric P + S vortex shedding at  $V_r = 6$  and  $f^* = 1$  is related to the additional  $1f_{oy}$  frequency component in the in-line motion and the oblique figure-eight trajectory.

The vortex shedding along the cylinder at  $V_r = 6$  and  $f^* = 2$  is displayed in Fig. 19. The vortex shedding at  $z/L = 0.25$  and  $0.75$  is in a 2P mode with two pairs of vortices being formed per cycle. Evidence of the 2P vortex shedding mode in free vibration was first exhibited by Brika and Laneville (1993, 1995). For the 2P mode at  $z/L = 0.25$ , the vortices are in pairs when they are shed from the cylinder. However, when the vortex pairs progress downstream, they split into multiple small scale vortices. The present observation agrees qualitatively with the CFD results of Zhao et al. (2014). In contrast, the vortex

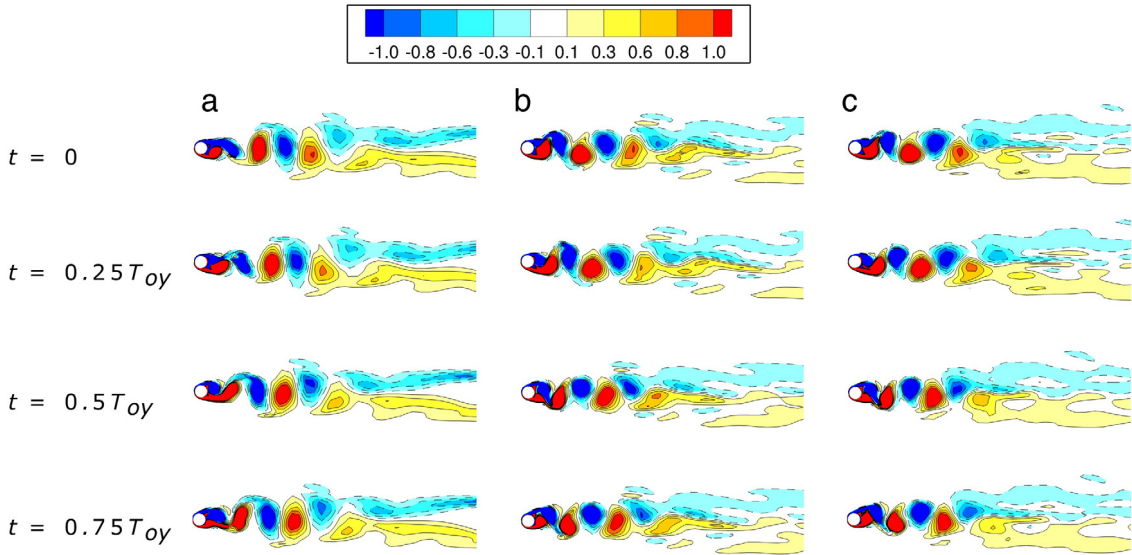


**Fig. 16.** Contours of spanwise vorticity  $\omega_z$  at different instants of time in one cross-flow vibration cycle on three cross sections along the cylinder at  $V_r = 3$  and  $f^* = 1$ : (a)  $z/L = 0.25$ , (b)  $z/L = 0.5$  and (c)  $z/L = 0.75$ .

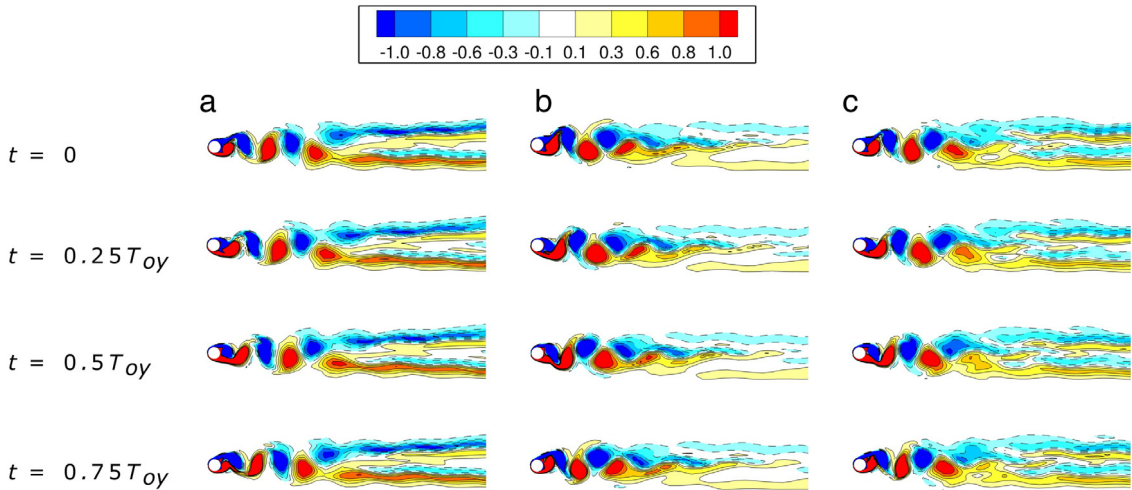


**Fig. 17.** Contours of spanwise vorticity  $\omega_z$  at different instants of time in one cross-flow vibration cycle on three cross sections along the cylinder at  $V_r = 3$  and  $f^* = 2$ : (a)  $z/L = 0.25$ , (b)  $z/L = 0.5$  and (c)  $z/L = 0.75$ .

pairs at  $z/L = 0.75$  similar to the flow visualisation results in the experiment by Govardhan and Williamson (2000) are more stable. At  $z/L = 0.5$ , a P + S mode resembling that in Bao et al. (2012) is observed.

In the instance where  $V_r = 9$  and  $f^* = 1$  (Fig. 20), the vortex shedding at  $z/L = 0.25$  exhibits a P + S mode and a 2P mode is observed at  $z/L = 0.5$  and  $0.75$ . As for  $V_r = 9$  and  $f^* = 2$ , as it appears in Fig. 21, although two pairs of vortices are shed in one cycle on the three cross sections, the vortex shedding patterns on the different cross sections are noticeably different.

The discussions above can be summarised as follows. When  $V_r = 3$  at  $f^* = 1$  and 2, the vortex shedding structures on the different cross sections are in phase and have similar 2S patterns, which leads to the well-organised distribution of  $C_L(z)$  along the cylinder and relatively large  $L_C/D$ . With the decrease of  $L_C/D$ , the variation of the vortex shedding patterns along the cylinder becomes apparent. This causes the relative phase shifts of the  $C_L(z)$  signals at different spanwise locations as mentioned in Section 4.6, and consequently results in a poor phasing between  $C_L(z)$  and  $y/D$ . According to Lucor et al. (2003, 2005), it is the poor phasing between the forces and the displacement that causes the decrease of  $L_C/D$ . As for the dominant vortex shedding mode in the cases with poor spanwise correlation, it modifies from a P + S mode to a 2P mode when  $f^*$  increases from 1 to 2 at  $V_r = 6$  and a 2P mode dominated vortex shedding is observed for both  $f^* = 1$  and 2 at  $V_r = 9$ .

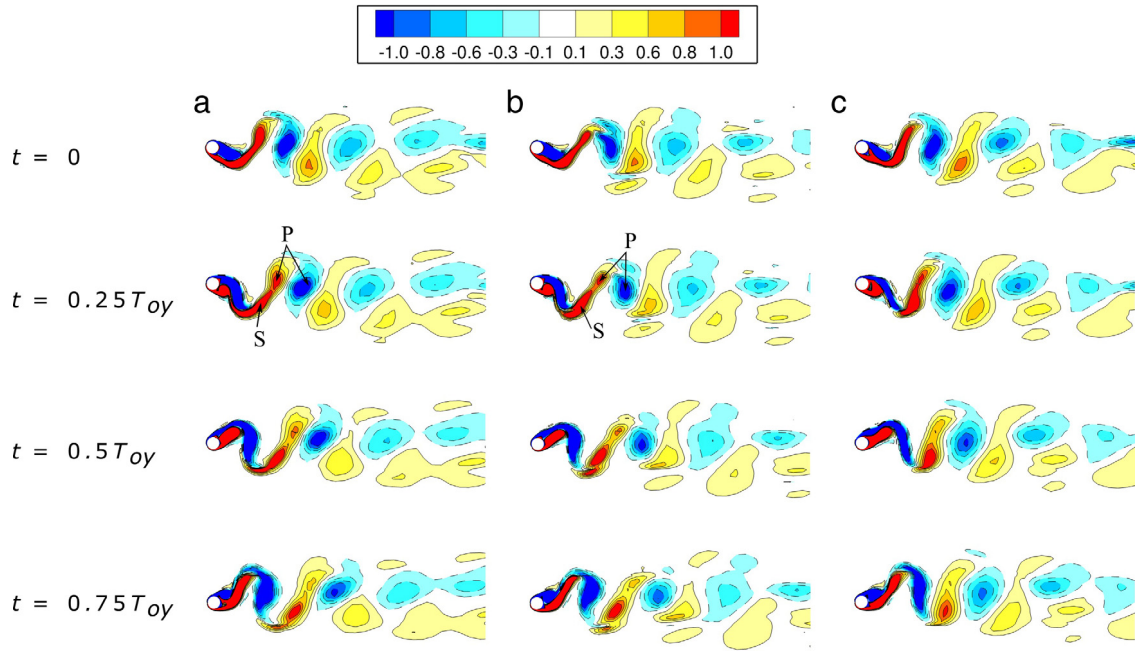


**Fig. 18.** Contours of spanwise vorticity  $\omega_z$  at different instants of time in one cross-flow vibration cycle on three cross sections along the cylinder at  $V_r = 6$  and  $f^* = 1$ : (a)  $z/L = 0.25$ , (b)  $z/L = 0.5$  and (c)  $z/L = 0.75$ .

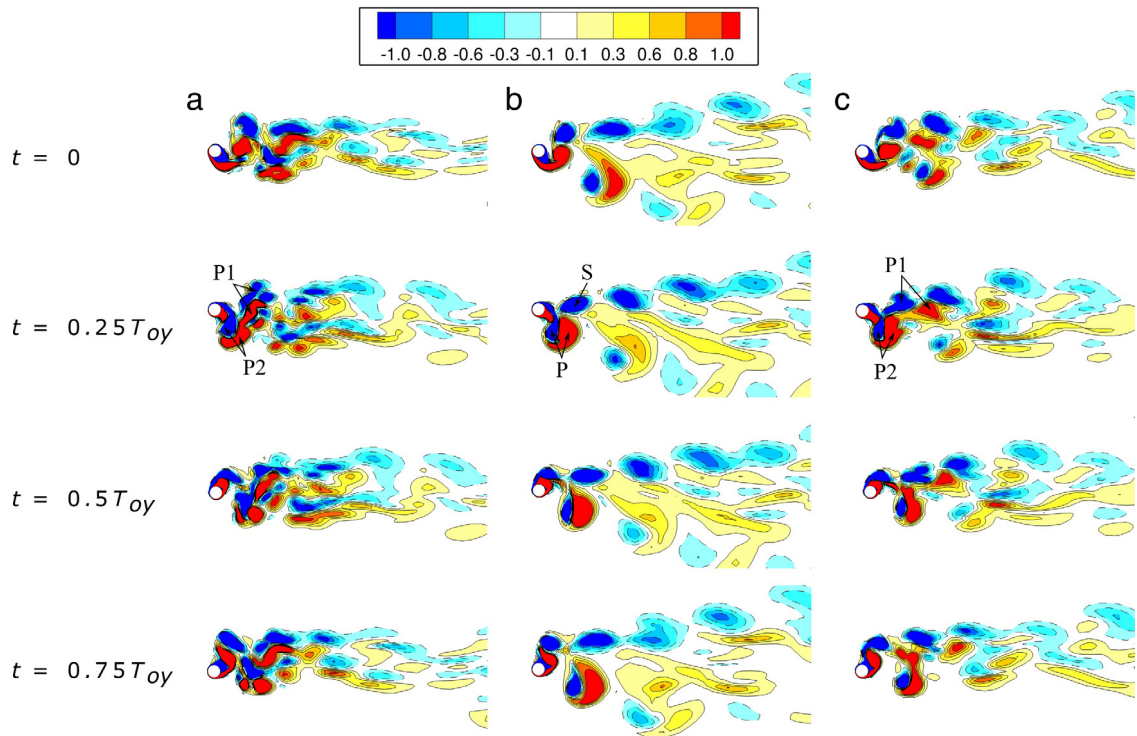


**Fig. 19.** Contours of spanwise vorticity  $\omega_z$  at different instants of time in one cross-flow vibration cycle on three cross sections along the cylinder at  $V_r = 6$  and  $f^* = 2$ : (a)  $z/L = 0.25$ , (b)  $z/L = 0.5$  and (c)  $z/L = 0.75$ .

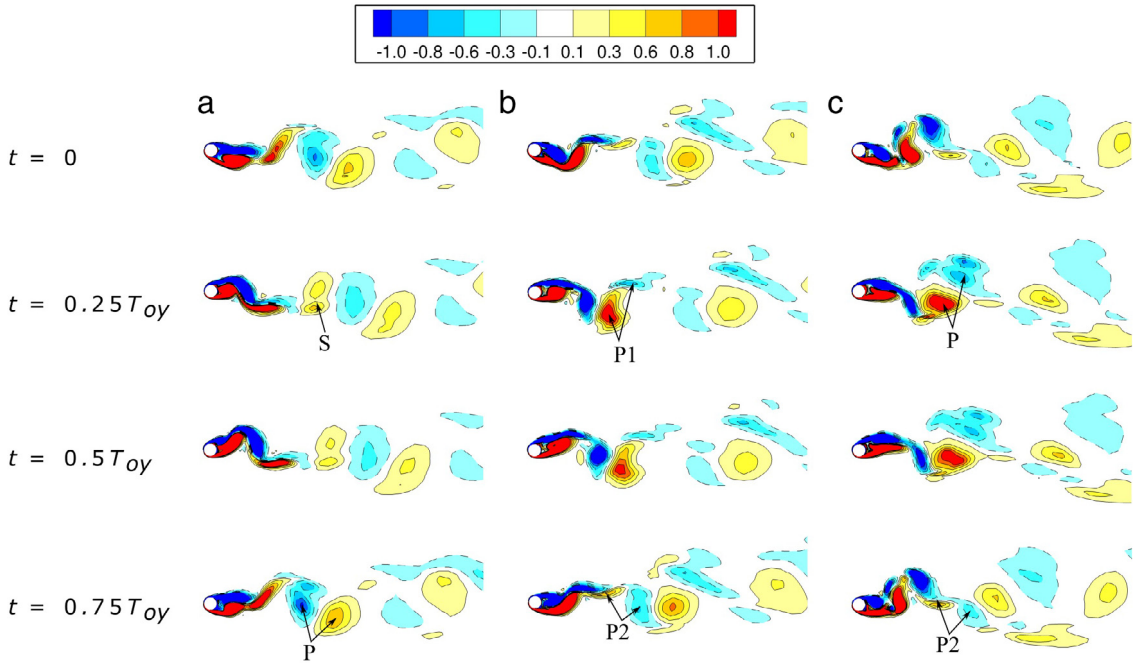


**Fig. 20.** Contours of spanwise vorticity  $\omega_z$  at different instants of time in one cross-flow vibration cycle on three cross sections along the cylinder at  $V_r = 9$  and  $f^* = 1$ : (a)  $z/L = 0.25$ , (b)  $z/L = 0.5$  and (c)  $z/L = 0.75$ .

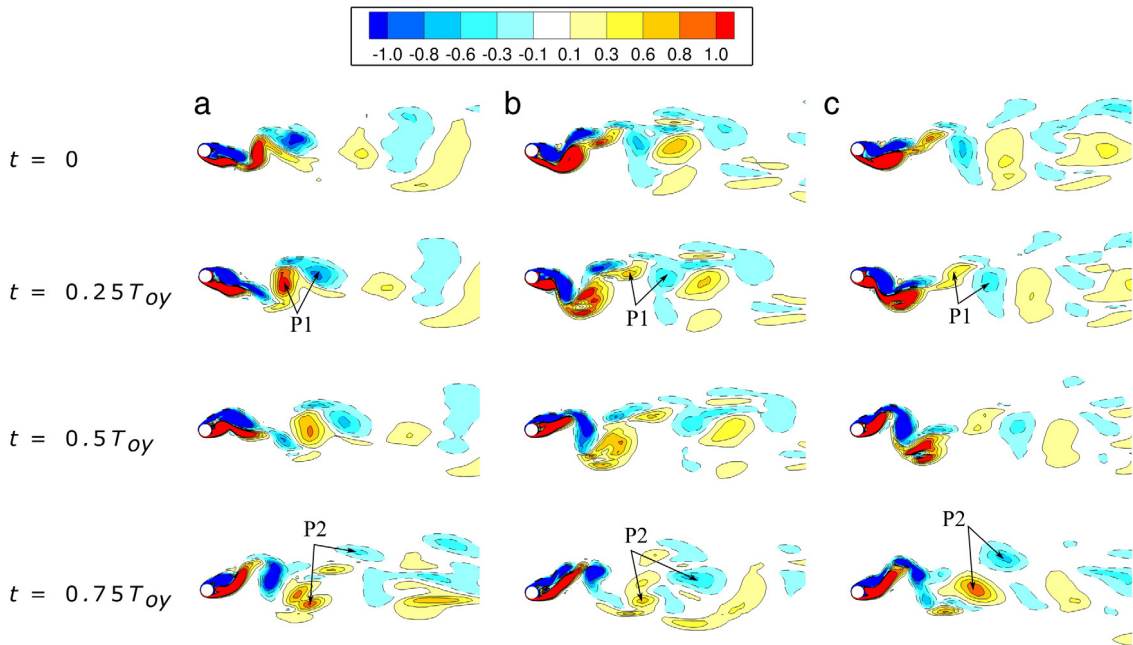


**Fig. 21.** Contours of spanwise vorticity  $\omega_z$  at different instants of time in one cross-flow vibration cycle on three cross sections along the cylinder at  $V_r = 9$  and  $f^* = 2$ : (a)  $z/L = 0.25$ , (b)  $z/L = 0.5$  and (c)  $z/L = 0.75$ .

**5. Conclusions**

The effect of  $f^*$  on 2DOF VIV of an elastically mounted circular cylinder is numerically studied at  $Re = 500$  using a 3D CFD method. A low mass ratio  $m^* = 2$  and zero structural damping are considered in the simulation. The  $V_r$  range is  $V_r = 2–12$  and  $f^*$  varies from 1 to 2 with an increment of 0.5. Based on the qualitative and quantitative analyses of the numerical results, the findings of this paper may be laid out as follows.

It is found that  $f^*$  has a significant impact on the  $A/D$  of the cylinder. In the present study,  $A_m/D$  increases and shifts to a higher  $V_r$  when  $f^*$  increases from 1 to 2. Where  $m_x^* = m_y^*$ , a single-peak cross-flow response is observed for  $f^* = 2$ . Dual resonance exists over a wide range of  $f^*$  with  $f_{ox}/f_{oy}$  being approximately 2 and most of the orbital trajectories having a figure-eight shape. The primary direction of the trajectories in the lock-in range is clockwise in which energy is transferred from the fluid to the body as a result of the closer proximity of the cylinder to the recently shed vortices. Conversely, the clockwise orbits are associated with damping fluid forces. The number of clockwise trajectories decreases as  $f^*$  increases.

$C_{Dmean}$  and  $C_{Drms}$  experience evident increases as  $f^*$  approaches 2 while  $C_{Lrms}$  is not quite sensitive to  $f^*$ . A third harmonic component is observed in  $C_L$  in the lock-in range. It is also found that with the increase of  $f^*$ , the third harmonic component becomes larger. The large third harmonic forces are found to be related to the counterclockwise motion of the cylinder. Due to the 2D feature of the flow, the displacements and hydrodynamic forces exhibit beating features. In terms of  $C_m$ , both  $C_{mx}$  and  $C_{my}$  decrease with the increase of  $V_r$ . As the variation of  $C_{mx}$  required to drive  $f_{ox}/f_{oy}$  to 2 is larger when  $f^*$  is distant from 2, the deviation in  $C_{mx}$  for different  $f^*$  is more obvious than that in  $C_{my}$ .

Large  $L_C/D$  is observed for low  $V_r$  in the pre-lock-in range which indicates the 2D characteristics of the flow.  $L_C/D$  experiences a decrease as  $V_r$  increases and reaches its minimum value at  $V_r$  near the transition region between the lock-in and post-lock-in ranges where the three-dimensionality of the flow is strongest. The decrease of  $L_C/D$  is due to the poor phasing between the forces and the displacement. After the trough,  $L_C/D$  begins to increase with increases of  $V_r$  in the post-lock-in range.

The vortex shedding is also found to be related to  $f^*$ . It is revealed that the wake in the lock-in range is wider than that in the non-lock-in range. The variation of the spanwise vortices is weaker when  $L_C/D$  is large. With the decrease of  $L_C/D$ , it becomes more difficult to identify the spanwise vortices. In the present study, three vortex shedding modes are observed, i.e., 2S, P + S and 2P modes. A 2S mode is observed at  $V_r = 3$  for both  $f^* = 1$  and 2. The vortex shedding structures on different spanwise cross sections are in phase with each other and the patterns are similar, which results in the strong correlation of  $C_L(z)$  at low  $V_r$  in the pre-lock-in range. At  $V_r = 6$ , variation of vortex shedding modes along the cylinder is observed. When  $f^* = 1$ , the vortex shedding is dominated by a P + S mode with a 2S mode appearing in the upper part of the cylinder. The asymmetric nature of the P + S mode is associated with the additional  $1f_{oy}$  frequency component in the in-line motion and the oblique figure-eight trajectory. The dominant vortex shedding mode switches to a 2P mode when  $f^* = 2$  with a P + S mode being observed on the middle section of the cylinder. When  $V_r$  is further increased to 9, the dominant vortex shedding mode for both  $f^* = 1$  and 2 is a 2P mode with a P + S mode being found in the lower part of the cylinder at  $f^* = 1$ . The variation of  $C_L(z)$  along the span is related to the variation of the vortex shedding flows.

## Acknowledgement

Results were obtained using the EPSRC funded ARCHIE-WeSt High Performance Computer ([www.archie-west.ac.uk](http://www.archie-west.ac.uk)). EPSRC grant no. EP/K000586/1.

## References

- ANSYS Inc., 2013. ANSYS CFX-Solver Theory Guide, Canonsburg, USA.
- Assi, G.R.S., Bearman, P.W., Kitney, N., 2009. Low drag solutions for suppressing vortex-induced vibration of circular cylinders. *J. Fluids Struct.* 25, 666–675.
- Bai, X., Qin, W., 2014. Using vortex strength wake oscillator in modelling vortex-induced vibration in two degrees of freedom. *Eur. J. Mech. B Fluids* 48, 165–173.
- Bao, Y., Huang, C., Zhou, D., Tu, J., Han, Z., 2012. Two-degree-of-freedom flow-induced vibrations on isolated and tandem cylinders with varying natural frequency ratios. *J. Fluids Struct.* 35, 50–75.
- Batcho, P., Karniadakis, G.E., 1991. Chaotic transport of two- and three-dimensional flow past a cylinder. *Phys. Fluids A* 3, 1051–1062.
- Bearman, P.W., 2011. Circular cylinder wakes and vortex-induced vibrations. *J. Fluids Struct.* 27, 648–658.
- Blevins, R.D., 1977. *Flow-Induced Vibration*. Van Nostrand Reinhold Company, New York, USA.
- Blevins, R.D., Coughran, C.S., 2009. Experimental investigation of vortex-induced vibration in one and two dimensions with variable mass, damping and Reynolds number. *J. Fluids Eng.* 131, 1–7.
- Bourguet, R., Karniadakis, G.E., Triantafyllou, M.S., 2013. Phasing mechanisms between the in-line and cross-flow vortex-induced vibrations of a long tensioned beam in shear flow. *Comput. Struct.* 122, 155–163.
- Bourguet, R., Modares-Sadeghi, Y., Karniadakis, G.E., Triantafyllou, M.S., 2011. Wake-body resonance of long flexible structures is dominated by counterclockwise orbits. *Phys. Rev. Lett.* 107, 1–4.
- Brika, D., Laneville, A., 1993. Vortex-induced vibrations of a long flexible circular cylinder. *J. Fluid Mech.* 250, 481–508.
- Brika, D., Laneville, A., 1995. An experimental study of the aeolian vibrations of a flexible circular cylinder at different incidences. *J. Fluids Struct.* 9, 371–391.
- Carmo, B.S., Meneghini, J.R., Sherwin, S.J., 2010. Possible states in the flow around two circular cylinders in tandem with separations in the vicinity of the drag inversion spacing. *Phys. Fluids* 22, 1–7.
- Dahl, J.M., Hover, F.S., Triantafyllou, M.S., 2006. Two-degree-of-freedom vortex-induced vibrations using a force assisted apparatus. *J. Fluids Struct.* 22, 807–818.
- Dahl, J.M., Hover, F.S., Triantafyllou, M.S., 2007. Resonant vibrations of bluff bodies cause multivortex shedding and high frequency forces. *Phys. Rev. Lett.* 99, 1–4.
- Dahl, J.M., Hover, F.S., Triantafyllou, M.S., 2008. Third harmonic lift forces from phase variation in forced crossflow and in-line cylinder motions. In: *Proceedings of the Ninth International Conference on Flow-Induced Vibrations*, Prague, Czech Republic.
- Dahl, J.M., Hover, F.S., Triantafyllou, M.S., Oakley, O.H., 2010. Dual resonance in vortex-induced vibrations at subcritical and supercritical Reynolds numbers. *J. Fluid Mech.* 643, 395–424.
- Facchinetti, M.L., de Langre, E., Biolley, F., 2004. Coupling structure and wake oscillators in vortex-induced vibrations. *J. Fluids Struct.* 19, 123–140.
- Farshidianfar, A., Zanganeh, H., 2010. A modified wake oscillator model for vortex-induced vibration of circular cylinders for a wide range of mass-damping ratio. *J. Fluids Struct.* 26, 430–441.

- Gabbai, R.D., Benaroya, H., 2005. An overview of modelling and experiments of vortex-induced vibrations of circular cylinders. *J. Sound Vib.* 282, 575–646.
- Gedikli, E.D., Dahl, J.M., 2014. Mode shape vibration for a low-mode number flexible cylinder subject to vortex-induced vibrations. In: *Proceedings of the ASME 33rd International Conference on Ocean, Offshore and Arctic Engineering*, San Francisco, USA.
- Govardhan, R., Williamson, C.H.K., 2000. Modes of vortex formation and frequency response for a freely-vibrating cylinder. *J. Fluid Mech.* 420, 85–130.
- Griffin, O.M., Ramberg, S.E., 1974. The vortex street wakes of vibrating cylinders. *J. Fluid Mech.* 66, 553–576.
- Gsell, S., Bourguet, R., Braza, M., 2016. Two-degree-of-freedom vortex-induced vibrations of a circular cylinder at  $Re = 3900$ . *J. Fluids Struct.* 67, 156–172.
- Guilmineau, E., Queutey, 2004. Numerical simulation of vortex-induced vibration of a circular cylinder with low mass-damping in a turbulent flow. *J. Fluids Struct.* 19, 449–466.
- Hover, F.S., Davis, J.T., Triantafyllou, M.S., 2004. Three-dimensional mode transition in vortex-induced vibrations of a circular cylinder. *Eur. J. Mech. B Fluids* 23, 29–40.
- Hover, F.S., Techet, A.H., Triantafyllou, M.S., 1998. Forces on oscillating uniform and tapered cylinders in crossflow. *J. Fluid Mech.* 363, 97–114.
- Huera-Huarte, F.J., Bearman, P.W., 2009. Wake structures and vortex-induced vibrations of a long flexible cylinder — Part I: Dynamic response. *J. Fluids Struct.* 25, 969–990.
- Hughes, T.J.R., 1987. *The Finite Element Method: Linear Static and Dynamic Finite Element Analysis*. Prentice-Hall, Inc., New Jersey, USA.
- Jauvtis, N., Williamson, C.H.K., 2004. The effect of two degrees of freedom on vortex-induced vibration at low mass and damping. *J. Fluid Mech.* 509, 23–62.
- Jeong, J., Hussain, F., 1995. On the identification of a vortex. *J. Fluid Mech.* 285, 69–94.
- Kang, Z., Jia, L., 2013. An experimental study of cylinder's two degree of freedom VIV trajectories. *Ocean Eng.* 70, 129–140.
- Khalak, A., Williamson, C.H.K., 1997. Fluid forces and dynamics of a hydroelastic structure with very low mass and damping. *J. Fluids Struct.* 11, 973–982.
- Khalak, A., Williamson, C.H.K., 1999. Motions, forces and mode transitions in vortex-induced vibration at low mass-damping. *J. Fluids Struct.* 13, 813–851.
- Kondo, N., 2012. Three-dimensional computation for flow-induced vibrations in in-line and cross-flow directions of a circular cylinder. *Internat. J. Numer. Methods Fluids* 70, 158–185.
- Leontini, J.S., Thompson, M.C., Hourigan, K., 2006. The beginning of branching behaviour of vortex-induced vibration during two-dimensional flow. *J. Fluids Struct.* 22, 857–864.
- Lucor, D., Foo, J., Karniadakis, G.E., 2003. Correlation length and force phasing of a rigid cylinder subject to VIV. In: Benaroya, H., Wei, T. (Eds.), *IUTAM Symposium on Integrated Modelling of Fully Coupled Fluid Structure Interactions Using Analysis, Computations and Experiments*. Springer, Dordrecht, pp. 187–199.
- Lucor, D., Foo, J., Karniadakis, G.E., 2005. Vortex mode selection of a rigid cylinder subject to VIV at low mass-damping. *J. Fluids Struct.* 20, 483–503.
- Lucor, D., Triantafyllou, M.S., 2008. Parametric study of a two degree-of-freedom cylinder subject to vortex-induced vibrations. *J. Fluids Struct.* 24, 1284–1293.
- Navrose, Mittal, S., 2013. Free vibrations of a cylinder: 3-D computations at  $Re = 1000$ . *J. Fluids Struct.* 41, 109–118.
- Paidoussis, M.P., Price, S.J., Langre, E., 2014. *Fluid-Structure Interactions: Cross-Flow-Induced Instabilities*. Cambridge University Press, New York, USA.
- Placzek, A., Sigrist, J., Hamdouni, A., 2009. Numerical simulation of an oscillating cylinder in a cross-flow at low Reynolds number: Forced and free oscillations. *Comput. & Fluids* 38, 80–100.
- Pontaza, J.P., Chen, H.C., 2006. Three-dimensional numerical simulations of circular cylinders undergoing two degree-of-freedom vortex-induced vibrations. *J. Offshore Mech. Arct. Eng.* 129, 158–164.
- Saltara, F., Neto, A.D., Lopez, J.I.H., 2011. 3D CFD simulation of vortex-induced vibration of cylinder. *Int. J. Offshore Polar Eng.* 21, 192–197.
- Sanchis, A., Sælevik, G., Grue, J., 2008. Two-degree-of-freedom vortex-induced vibrations of a spring-mounted rigid cylinder with low mass ratio. *J. Fluids Struct.* 24, 907–919.
- Sarpkaya, T., 1995. Hydrodynamics damping, flow-induced oscillations and biharmonic response. *J. Offshore Mech. Arct. Eng.* 117, 232–238.
- Singh, S.P., Mittal, S., 2005. Vortex-induced oscillations at low Reynolds numbers: Hysteresis and vortex shedding modes. *J. Fluids Struct.* 20, 1085–1104.
- Srinil, S., Rega, G., 2007. Two-to-one resonant multi-modal dynamics of horizontal/inclined cables: Part II: Internal resonance activation, reduced-order models and nonlinear normal modes. *Nonlinear Dynam.* 48, 253–274.
- Srinil, N., Rega, G., Chucheepsakul, S., 2007. Two-to-one resonant multi-modal dynamics of horizontal/inclined cables. Part I: Theoretical formulation and model validation. *Nonlinear Dynam.* 48, 231–252.
- Srinil, N., Zanganeh, H., 2012. Modelling of coupled cross-flow/in-line vortex-induced vibrations using double Duffing and van der Pol oscillators. *Ocean Eng.* 53, 83–97.
- Srinil, N., Zanganeh, H., Day, A., 2013. Two-degree-of-freedom VIV of a circular cylinder with variable natural frequency ratio: Experimental and numerical investigations. *Ocean Eng.* 73, 179–194.
- Stappenbelt, B., Lalji, F., Tan, G., 2007. Low mass ratio vortex-induced motion. In: *Proceedings of the 16th Australasian Fluid Mechanics Conference*, Gold Coast, Australia.
- Sumer, B.M., Fredsøe, J., 2006. *Hydrodynamics Around Cylindrical Structures*. World Scientific Publishing Co. Pte. Ltd., London, UK.
- Swithenbank, B.S., Vandiver, J.K., Larsen, C.M., Lie, H., 2008. Reynolds number dependence of flexible cylinder VIV response data, OMAE2008-57045. In: *Proceedings of the ASME 27th International Conference on Offshore Mechanics and Arctic Engineering*, Estoril, Portugal.
- Tognarelli, M.A., Slocum, S.T., Frank, W.R., Campbell, R.B., 2004. VIV response of a long flexible cylinder in uniform and linearly sheared currents, OTC 16338. In: *Proceedings of the 2004 Offshore Technology Conference*, Houston, USA.
- Vandiver, J.K., Jong, J.Y., 1987. The relationship between in-line and cross-flow vortex-induced vibration of cylinders. *J. Fluids Struct.* 1, 381–399.
- Wang, E., Xiao, Q., 2016. Numerical simulation of vortex-induced vibration of a vertical riser in uniform and linearly sheared currents. *Ocean Eng.* 121, 492–515.
- Williamson, C.H.K., 1988. The existence of two stages in the transition to three-dimensionality of a cylinder wake. *Phys. Fluids* 31, 3165–3168.
- Williamson, C.H.K., 1989. Oblique and parallel modes of vortex shedding in the wake of a circular cylinder at low Reynolds number. *J. Fluid Mech.* 206, 579–627.
- Williamson, C.H.K., Govardhan, R., 2004. Vortex-induced vibrations. *Annu. Rev. Fluid Mech.* 36, 413–455.
- Williamson, C.H.K., Roshko, A., 1988. Vortex formation in the wake of an oscillating cylinder. *J. Fluids Struct.* 2, 355–381.
- Wu, J., Lie, H., Larsen, C.M., Liapis, S., Baarholm, R., 2016. Vortex-induced vibration of a flexible cylinder: Interaction of the in-line and cross-flow responses. *J. Fluids Struct.* 63, 238–258.
- Zanganeh, H., Srinil, N., 2014. Characterization of variable hydrodynamic coefficients and maximum responses in two-dimensional vortex-induced vibrations with dual resonance. *J. Vib. Acoust.* 136, 1–15.
- Zdera, R., Turan, Ö.F., Havard, D.G., 1995. Towards understanding galloping: Near-wake study of oscillating smooth and stranded circular cylinders in forced motion. *Exp. Therm Fluid Sci.* 10, 28–43.
- Zhao, M., Cheng, L., 2011. Numerical simulation of two-degree-of-freedom vortex-induced vibration of a circular cylinder close to a plane boundary. *J. Fluids Struct.* 27, 1097–1110.
- Zhao, M., Cheng, L., An, H., Lu, L., 2014. Three-dimensional numerical simulation of vortex-induced vibration of an elastically mounted rigid circular cylinder in steady current. *J. Fluids Struct.* 50, 292–311.